UNIVERSITAT DE BARCELONA

Non-Equilibrium Dynamics of Driven and Confined Colloidal Systems

Eric Cereceda López

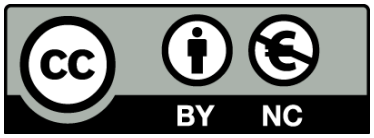

Non-Equilibrium Dynamics of Driven and Confined Colloidal Systems

Doctoral Thesis

Eric Cereceda López

University of Barcelona
Departament de Física de la Matèria Condensada

UNIVERSITAT DE BARCELONA

Non-Equilibrium Dynamics of Driven and Confined Colloidal Systems

Memòria presentada per optar al grau de doctor per la
Universitat de Barcelona

Autor:
Eric Cereceda López

Directors:
Prof. Pietro Tierno
Prof. Antonio Ortiz Ambriz

Tutor:
Prof. Giancarlo Franzese

UNIVERSITAT DE BARCELONA

"All we have to decide is what to do with the time that is given to us"
— J. R. R. Tolkien, The Fellowship of the Ring

Abstract

In this thesis, I investigate the collective dynamics of confined colloidal particles dispersed in water and driven through an optical potential. For this purpose, I used micro-meter size polystyrene particles, which I arrange in the optical potential created by fast scanning optical tweezers.

With the help of an Acousto Optical Deflector (AOD), which varies the laser position at a high frequency, I created multiple quasi-simultaneous optical traps. With this technique, it was possible to manipulate the particles and vary with high precision the parameters of the optical potential. During the experiments, I recorded videos of the particles' dynamics using optical microscopy. Thus, I obtained the particles' positions over time, which allows me to measure different quantities with the aim at the mechanisms of the forced transport.

The results presented in this thesis highlight the importance of Hydrodynamic Interactions (HI) when the transport of particles occurs due to a fluid drag. In addition, different situations are compared, including the change in the relative particle size with respect to the separation between potential wells. In addition, I demonstrated the emergence of solitons propagating with high speed against the direction of the drag force. This situation, which appears when the system is overcrowded, i.e., the number of particles exceed that of potential wells, presents a novel mechanism to transport and spread matter at the microscale.

Resumen en Castellano

En esta tesis investigo la dinámica colectiva de partículas coloidales dispersas en agua cuando son forzadas a moverse a través de un potencial óptico. Para ello, utilizo partículas de poliestireno de tamaño micrométrico, las cuales dispongo en el potencial óptico creado con un sistema de pinzas ópticas.

Con la ayuda de un Deflector Acusto Óptico (AOD), el cual varía la posición del láser a una alta frecuencia, he creado múltiples trampas ópticas de manera casi simultánea. Esto me permite manipular las partículas con facilidad y variar con una alta precisión los parámetros del potencial óptico. A través de microscopía óptica, obtengo imágenes en vídeo de la dinámica de las partículas. Así, obtengo la posición de las partículas a lo largo del tiempo, lo que me permite medir diferentes parámetros para determinar los mecanismos que se desarrollan durante el transporte forzado de las partículas.

Los resultados expuestos en esta tesis ponen de manifiesto la importancia de las Interacciones Hidrodinámicas (HI) en el transporte de partículas cuando son arrastradas por el fluido. Además, se comparan diferentes situaciones en las que se incluye el cambio en el tamaño relativo de las partículas respecto a la separación entre pozos de potencial. Además, demuestro la aparición de solitones que se propagan a alta velocidad en dirección contraria a la fuerza de arrastre. Esta situación, que aparece al sobrepoblar el sistema, es decir, el número de partículas es mayor al número de pozos de potencial, presenta un novedoso mecanismo para transportar materia a escala micrométrica.

Resum en Català

En aquesta tesi investigo la dinàmica col·lectiva de partícules col·loidals disperses en aigua quan són forçades a moure's a través d'un potencial òptic. Per a això, utilitzo partícules de poliestirè de grandària micromètric, les quals disposo en el potencial òptic creat amb un sistema de pinces òptiques.

Amb l'ajuda d'un Deflector Acusto Òptic (AOD), el qual varia la posició del làser a una alta freqüència, he creat múltiples paranys òptics de manera gairebé simultània. Això em permet manipular les partícules amb facilitat i variar amb una alta precisió els paràmetres del potencial òptic. A través de microscòpia òptica, obtinc imatges en vídeo de la dinàmica de les partícules. Així, aconsegueixo la posició de les partícules al llarg del temps, la qual cosa em permet mesurar diferents paràmetres per a determinar els mecanismes que es desenvolupen durant el transport forçat de les partícules.

Els resultats exposats en aquesta tesi posen de manifest la importància de les Interaccions Hidrodinàmiques (HI) en el transport de partícules quan són arrossegades pel fluid. A més, es comparen diferents situacions en les quals s'inclou el canvi en la grandària relativa de les partícules respecte a la separació entre pous de potencial. A més, demostro l'aparició de solitons que es propaguen a alta velocitat en direcció contrària a la força d'arrossegament. Aquesta situació, que apareix al sobre poblar el sistema, és a dir, el nombre de partícules és major al nombre de pous de potencial, presenta un nou mecanisme per a transportar matèria a escala micromètrica.

Contents

Chapter 1

Introduction

Nowadays, science and technology are growing at the highest speed humanity has ever witnessed. Since scientific progress allows fast technological development, we need a better understanding of the most fundamental processes occurring in nature. This picture is common in most fields of science where, in many situations, these processes, although uncorrelated, share similar physical principles.

However, it is very challenging to study these systems; nature and human-made developed devices are complex systems where we find multiple elements interacting simultaneously, so it is hard to extract solid analyses of the specific mechanisms we pretend to investigate. For this goal, we need to discern among all the events occurring in the system and obtain information about the governing physical laws.

We should avoid all the external actors that interfere with the observation to make a proper analysis without dealing with superfluous information. This way, we can go to the fundamental phenomenon, obtaining valuable information that would help us understand the basics of the physical process. We can assemble our laboratories' artificial systems with specific conditions where we keep only the interactions we desire to examine. These assemblies are called model systems and are usually a convenient way of extracting useful information about specific phenomena that are too complex to investigate

directly. The utility of model systems arises from their easy manipulation, versatility, and the possibility to determine all the degrees of freedom of the system.

In this thesis, I show how I used colloidal particles manipulated with optical tweezers to explore the multi-particle dynamics in driven-confined microscale systems. I present several results obtained from investigations in colloidal model systems. Model systems based on colloidal particles are suitable to mimic more complicated scenarios, like the dynamics of collections of atoms or molecules. As I show in Chapter 2, colloidal model systems are versatile, easy to observe directly to obtain direct information with conventional optical microscopy, and easy to manipulate. Moreover, one can synthesize colloids to obtain different interactions between particles (for example, hard-core, electric, or magnetic) and, thus, reproduce a great variety of physical situations.

1.1 Thesis aim and outline

The main objective of this thesis is to explore the emerging processes occurring when confined systems of colloidal particles are driven by external fields. In particular, I expose the importance of collective phenomena arising in neutral multi-particle systems, where the main interaction between the particles is collisions. I also investigate the importance of the dispersing medium, particularly I explore the role of a fluid environment in the interaction between colloidal particles in suspension. The conclusions I draw in this thesis can be interesting for microfluidic applications, the development of lab-on-a-chip devices, and the understanding of different biological processes.

The thesis is structured as follows. In Chapter 2 and Chapter 3, I introduce the fundamentals of colloid science and the principles of optical tweezers, respectively. There, I provide the basis to understand the physics of the model systems I used in this work. In Chapter 4, I present the equipment I have used to realize the experimental part of this thesis and the software tools I used to retrieve the experimental data and develop the analysis.

In Chapters 5, 6, and 7, I describe the experimental systems I used to

explore the multi-particle dynamics of confined colloidal particles driven across periodic potential landscapes.

Finally, in Chapter 8, I recapitulate the main results obtained in these works, make an overall conclusion of the thesis, and give some possible paths to continue in the future the research line I have started.

Chapter 2

Fundamentals of Colloid Science

Colloidal suspensions are present in our daily lives. We can encounter them in soaps (colloidal electrolytes), milk (emulsion), fog (aerosol), jelly (sol), or beer (foam). Colloidal suspensions are systems composed of dispersed particles in a homogeneous immiscible medium. The solute particles are much larger than those of the solvent molecules. Typically, the particle size of the solute has diameters in the range of 10 to 10000 nanometers.

Besides the importance of colloidal suspensions in our day-to-day life, they are also of enormous relevance in multiple technological fields, where scientists widely study them in chemistry and physics laboratories [1]. We could identify the origin of modern colloidal science in the early nineteenth century with the work of Thomas Graham (1805-1869), that systematically studied polysaccharide gums and, in turn, gave the name 'colloid' to these substances, which comes from the ancient Greek word 'kolla' and means gum-like [2–5]. In his work [6], he first describes two classes of matter: crystalloids, including salt, sugar, and other substances that crystallize, and colloids, which in contrast, do not crystalize like albumin, gum arabic, or gelatin.

Later on, Robert Brown (1773-1858) described the erratic motion of clay

particles suspended in water, observed from his experiments on a suspension of pollen from *Clarika Pulchella* whose cytoplasm contained particles of about 5 μm diameter [7]. This random movement of the particles in suspension is nowadays known as Brownian motion.

2.1 Brownian motion

In Robert Brown's work, he first observed the random movement of microscopic objects suspended in a fluid medium. However, the investigation of Jean Perrin (1870-1942) settled the basis for understanding molecular motion. Perrin reported how particles seem to move independently with no effect of density or composition and noticed that the movement amplitude is higher for smaller particles, decreases with the medium viscosity, and increases with temperature [8]. Jean Perrin and Louis G. Gouy (1854-1926), who performed experiments isolating the system from any external noise source like mechanical vibrations [9], attributed the jiggling motion of the particles to the ceaseless impacts of the fluid molecules. They determined that the energy transfer between the solvent molecules and the solute particles was equal to $\frac{3}{2}k_BT$ [10], where k_B is the Boltzmann constant and T is the absolute temperature. This assumption agrees with the observation done by Perrin that smaller particles and higher temperatures promote larger amplitudes of motion.

On the other hand, Paul Langevin (1872-1946) developed the mathematical description of the motion dynamics of individual particles performing Brownian motion. Consider a colloid as a neutral spherical particle of radius a in a fluid of viscosity η and density ρ. Since it is impossible to precisely describe the multiple collisions of the fluid molecules with the colloidal particle, one has to adopt a continuum approach when considering the dispersing medium. In particular, one can approximate all these collisions as a single random force acting over the particle that induces Brownian motion.

Applying the second Newton's law to a particle in suspension in a fluid, we reach the Langevin equation:

$$m\frac{\mathrm{d}^2\vec{r}}{\mathrm{d}t^2} = \vec{\zeta}(t) - 6\pi\eta a\frac{\mathrm{d}\vec{r}}{\mathrm{d}t} \tag{2.1}$$

There, m is the particle mass ($m = \frac{4}{3}\pi a^3\rho$) and $\vec{r}(t)$ is the particle position. Hence, the effect of the external random force $\vec{\zeta}(t)$, along with the friction force produced by the fluid viscosity, results in the acceleration of the particle. In equation (2.1), the last term on the right-hand side is the friction force of the fluid, where $\gamma = 6\pi\eta a$ is the Stokes coefficient for a spherical particle, the inverse of the mobility μ.

To complete the integration of the Langevin equation, we need to define the random force $\vec{\zeta}$ to match the experimental observations. Brownian forces act randomly in direction and magnitude and are δ correlated in time. Mathematically, this corresponds to:

$$\begin{aligned} \left\langle \vec{\zeta}(t) \right\rangle &= 0 \\ \left\langle \vec{\zeta}(t)\vec{\zeta}(t+\tau) \right\rangle &= \vec{K}\delta(\tau) \end{aligned} \tag{2.2}$$

Now $\delta(\tau)$ is the Dirac delta function with properties $\delta(\tau) = 0$, for $\tau \neq 0$, and $\int_{-\infty}^{\infty}\delta(\tau)\,\mathrm{d}\tau = 1$ [11]. These conditions of Eqs. (2.2) are also characteristic of white noise [12]. Equation (2.1) is the prototype of a stochastic differential equation, which has many other applications in science due to its versatility in the description of noise in general systems [13].

In the case of Brownian motion, the constant vector $\vec{K}$ is given by $\vec{K} = 2\gamma k_B T\vec{n}$ [10, 13], where $\vec{n}$ is the unit vector. This result derives from the energy equipartition theorem, and Perrin demonstrated that it applies not only to the liquid molecules but also to colloids [14].

We have finally described the dynamics of the Brownian motion for a spherical particle in a fluid suspension. Nevertheless, it is still challenging to precisely determine the particle position in time due to the stochastic noise in equation (2.1). Thus one can only obtain relevant information about this process from statistical analysis. Therefore, in the following section, we study this statistical process by treating the displacements produced by the Brownian random forces like a diffusion process.

2.2 Diffusion of colloidal particles

We are now interested in studying Brownian motion from the point of view of a diffusion process. Albert Einstein (1879-1955) developed this idea in the early 20th-century [15, 16] and provided the theoretical description of the work performed by Perrin [10], who was also capable of estimating the Avogadro constant using Einstein's relation [2, 3]. One of the results derived from the investigations of Albert Einstein is the Sotkes-Einstein relation of diffusion, which establishes a connection between the diffusion coefficient and the drag coefficient of the fluid:

$$D = \frac{k_B T}{\gamma} \tag{2.3}$$

The Stokes-Einstein relation applies to the diffusion of a spherical particle on a fluid with a low Reynolds number, which would be the situation for a colloidal particle suspended in water.

In the following, we restrict ourselves to one-dimensional analysis for simplicity, as the extension to more dimensions is straightforward. We are interested in obtaining the mean-squared displacement ($\langle x^2 \rangle$), which gives valuable information about the system's dynamics. To do so, we first multiply Eq. (2.1) by x and take the averages using the Gaussian random noise property of Eq. (2.2):

$$m\frac{d\langle x\dot{x}\rangle}{dt} = m\langle \dot{x}^2 \rangle - \gamma \langle x\dot{x}\rangle \tag{2.4}$$

where we have also applied the equality $mx\ddot{x} = m\left[\frac{d(x\dot{x})}{dt} - \dot{x}^2\right]$. Since the dispersing medium is at the thermodynamic equilibrium, the kinetic energy of the fluid molecules follows the equipartition theorem, $m\langle \dot{x}^2 \rangle /2 = k_B T/2$, and Eq. (2.4) takes the form:

$$\left(\frac{d}{dt} + \frac{\gamma}{m}\right)\langle x\dot{x}\rangle = \frac{k_B T}{m} \tag{2.5}$$

Whose solution is

$$\langle x\dot{x}\rangle = \frac{1}{2}\frac{d\left\langle x^2\right\rangle}{dt} = Ce^{-\frac{\gamma t}{m}} + \frac{k_B T}{\gamma} \tag{2.6}$$

C is a derivative constant, which we can determine by applying the boundary conditions. In our case, the mean square displacement is zero at the initial time $t = 0$, hence $0 = C + \frac{k_B T}{\gamma}$ and Eq. (2.6) becomes:

$$\frac{1}{2}\frac{d\left\langle x^2\right\rangle}{dt} = \frac{k_B T}{\gamma}\left(1 + e^{-\frac{\gamma t}{m}}\right) \tag{2.7}$$

On integrating Eq. (2.7) we find:

$$\left\langle x^2\right\rangle = \frac{2k_B T}{\gamma}\left[t - \frac{m}{\gamma}\left(e^{-\frac{\gamma t}{m}} - 1\right)\right] \tag{2.8}$$

Which, considering that the times are much longer than the viscous relaxation times ($t \gg \rho a^2/\eta$, or the same that $t \gg m/\gamma$), finally leads to

$$\left\langle x^2(t)\right\rangle = 2\frac{k_B T}{\gamma}t = 2Dt \tag{2.9}$$

For the three dimensional case, if the medium is at equilibrium and isotropic, to obtain the mean square displacement is straightforward from the one dimensional case since $\left\langle r^2\right\rangle/3 = \left\langle x^2\right\rangle$ and so:

$$\left\langle r^2(t)\right\rangle = 6Dt \tag{2.10}$$

2.3 Interaction between Colloids

Until now, we have only considered the diffusion of individual colloids, but many intriguing phenomena arise from the collective interactions between particles. Since colloidal particles are in a fluid suspension, typically in water, there is an effective interaction between individual particles with liquid molecules and ions.

Usually, dispersed particles acquire a net charge on their surface for different reasons: a metal oxide nature or a defect structure on their crystals,

which generates the presence of surface groups [2]. Hence, when colloidal particles are in a liquid suspension, we expect the ions in the fluid with opposite charges to be closer to the particle's surface. The arrangement of ionic charges around the colloidal particles is known as the diffuse electric double layer.

Now, if two colloidal particles are close to each other, a repulsive force arises between them due to the compression of the electric double layer. However, there are also attractive forces between colloids that may bring them together. In some scenarios, individual colloidal particles can collide to form an aggregate, so the system is unstable. The process of colloidal aggregation can occur via flocculation (reversible) or coagulation (irreversible) [2]. The attraction between colloids can be due to long-ranged van der Waals forces, which originates from molecular interactions [3].

The balance between repulsive-attractive forces determines the stability and dynamics of the colloidal suspension. The work of Boris Derjaguin (1902-1994) and Lev Landau (1908-1968) first [17], and the later interpretation by Jan Theodor Gerard Overbeek (1911-2007) and Evert Johannes Willen Verwey (1905-1981) [18, 19] gave rise to the DLVO theory, which describes the total electrostatic interaction between particles. Indeed, the DLVO theory expands and completes the work of Louis Georges Gouy [20] and David Leonard Chapman (1869-1958) [21], who extensively studied the diffusive double layer, establishing the well-known Gouy-Chapman model with their investigation.

Figure 2.1 shows a plot representing the different types of interaction energy involved between charged surfaces. The DLVO interaction potential is the sum of the double-layer repulsion and the van der Waals attraction, which varies depending on the surface charge of the particles in the solution. The DLVO potential is recognized for providing an accurate description of long-range interaction forces between similarly charged particles [22].

2.3.1 Hydrodynamic Interactions

The Hydrodynamic Interactions (HI) between colloidal particles dispersed in water emerge from the movement of the fluid produced by their diffusive or

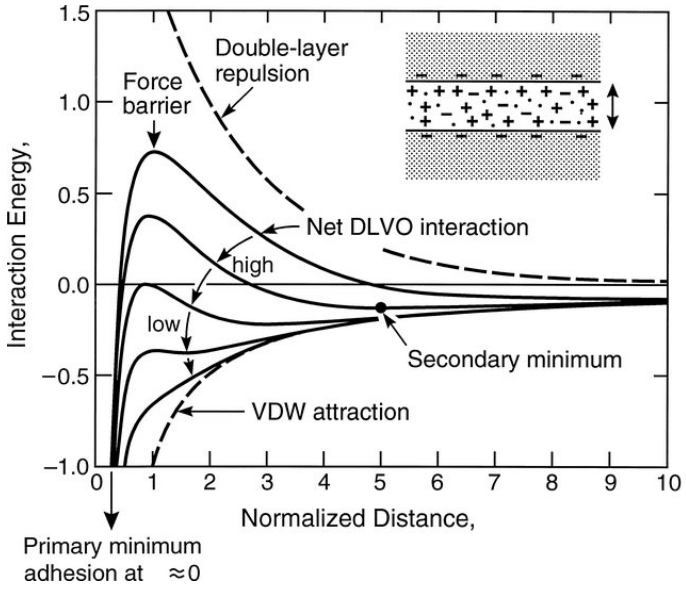

Figure 2.1: Representation of the repulsive double-layer potential (upper dashed line), the Van der Waals (VDW) attractive interaction (lower dashed line), and the DLVO potential (solid lines) that determine the net interaction between two charged surfaces immersed in aqueous solution for different surface charges. [22]

driven motion. In many situations, the dispersing medium is an incompressible Newtonian fluid, such as water, whose motion obeys the Navier-Stokes equations:

$$\nabla \cdot \vec{u} = 0 \tag{2.11}$$

$$\rho \left(\frac{\partial \vec{u}}{\partial t} + \vec{u} \cdot \nabla \vec{u} \right) = -\nabla p + \eta \nabla^2 \vec{u} \tag{2.12}$$

Where $\vec{u}$ is the fluid velocity, p is the dynamic pressure, and η is the

shear viscosity, constant for Newtonian fluids such as water.

We can further simplify Eqs. (2.11) and (2.12) by considering that colloidal particles are usually at low Reynolds numbers. The Reynolds number ($Re \equiv \frac{\rho u L}{\eta}$, where L is a characteristic linear dimension) provides an estimate of the importance of inertia relative to viscous forces. Thus, if we consider 2 μm radius particle, which moves in water at room temperature at a speed of 10^{-5} m/s, the Reynolds number is negligible ($Re \approx 10^{-5}$). Hence, in this scenario, we can neglect the inertia term and assume steady conditions, which simplifies equation (2.12) to:

$$\nabla p = \eta \nabla^2 \vec{u} \tag{2.13}$$

This equation is the Stokes equation. For a sphere at rest, we can extract the drag a fluid exerts ($\vec{F}$) when it moves at speed $\vec{u}_f$ by solving the Stokes equations computing the stress tensor and integrating over the sphere surface [10]. This gives rise to Stokes law:

$$\vec{F} = 6\pi\eta a \vec{u}_f \quad \text{or} \quad = -6\pi\eta a \vec{U}_0 \tag{2.14}$$

In which we can identify the mobility of a sphere $\mu = \frac{1}{6\pi\eta a}$.

Solving the Stokes equations (Eqs. 2.11 and 2.13), it is possible to find the mobility tensors that describe the interaction between particles due to the fluid presence between them [23–25]. We will restrict the discussion to the experimental conditions of this thesis, where we find that particles are near a planar boundary, then we will apply the no-slip boundary condition.

The single particle case can be solved using the method of images and leads to the Blake tensor $\vec{\mu}^B$ [26]. To obtain the interaction between two particles of radius a at positions r_i and r_j, one has to perform a multipole expansion to the second order of the Blake tensor. The result is the Blake tensor at the Rotne-Prager level [27], which decomposes into a self and an interaction part:

$$\vec{\mu}_{ij} = \vec{\mu}^{RPB}_{self}(z_i)\delta_{ij} + (1 - \delta_{ij})\vec{\mu}^{RPB}(\vec{r}_i, \vec{r}_j) \tag{2.15}$$

The self component depends only on the distance z of a particle from the coverslip surface,

$$\vec{\mu}_{self}^{RPB}(z) = \begin{pmatrix} \vec{\mu}_{\parallel}^{RPB}(z) & 0 & 0 \\ 0 & \vec{\mu}_{\parallel}^{RPB}(z) & 0 \\ 0 & 0 & \vec{\mu}_{\perp}^{RPB}(z) \end{pmatrix} \tag{2.16}$$

Where the self-mobility tensors parallel ($\vec{\mu}_{\parallel}^{RPB}$) and perpendicular ($\vec{\mu}_{\perp}^{RPB}$) to the wall are [28]:

$$\vec{\mu}_{\parallel}^{RPB} = \mu \left(1 - \frac{9a}{16z} + \frac{1}{8}\left(\frac{a}{z}\right)^3\right) \tag{2.17}$$

$$\vec{\mu}_{\perp}^{RPB} = \mu \left(1 - \frac{9a}{8z} + \frac{1}{2}\left(\frac{a}{z}\right)^3\right) \tag{2.18}$$

The interaction contribution proceeds from the second-order term of the multipole expansion of the Blake tensor:

$$\vec{\mu}^{RPB}(\vec{r}_i, \vec{r}_j) = \left(1 + \frac{a^2}{6}\nabla_{\vec{r}_i}^2 + \frac{a^2}{6}\nabla_{\vec{r}_j}^2\right) \vec{\mu}^{B}(\vec{r}_i, \vec{r}_j) \tag{2.19}$$

The mobility tensors show that the self-mobilities of the spheres moving near planar boundaries depend on the ratio between the sphere radius (a) and the distance to the wall (z). Moreover, the mobility of the spheres diffusing parallel to the wall is higher than that obtained when moving perpendicular to the boundary ($\vec{\mu}_{\parallel}^{RPB} > \vec{\mu}_{\perp}^{RPB}$).

We know that, at high densities, particles interact through long-range HI, which are mediated by the flow of the dispersing medium [29–31]. These interactions decay as $1/r$ (r is the distance between two neighboring spheres $r = |\vec{r}_i - \vec{r}_j|$) in an unbounded fluid. When the particles move along the direction parallel to a close wall, the HI become weaker, and it decays as $1/r^3$ for particles at distances farther than their separation with the wall ($|\vec{r}_i - \vec{r}_j| \gg z$). In the case of particles moving perpendicular to the surface, the HI strength decays much faster, proportional to $1/r^5$ [28]. For two touching particles at a distance $z = 2a$ from a wall, the HI strength gets reduced by 20% [28]. Nevertheless, we cannot neglect the HIs until we reach the limit of large distances ($|\vec{r}_i - \vec{r}_j| > 100a$), thus they are of fundamental importance in transport phenomena as we will discuss in Chapter 5.

2.4 Colloids as Model Systems

One could think that the physics of colloidal systems is well understood, but there is still much to understand and explore on their collective dynamics. Model systems are well-controlled systems easy to manipulate, which we can use to reproduce and understand more complicated effects on different lengths and time scales. Indeed, they are helpful because we acquired a good comprehension of the physical laws governing these model systems, but other reasons make colloids relevant in this type of investigation.

When I introduced the Brownian motion of colloidal particles, I did not mention that the energy equipartition theorem in a fluid suspension is fulfilled. This discovery had tremendous importance in modern science and is considered the keystone of using colloids as model systems [14]. Hence, a collection of colloids is equivalent to its counterpart of atoms or molecules from the thermodynamic or statistical physics point of view.

One could think that if we are interested in studying in detail the behavior of molecular systems, there is no reason to study colloids. Unfortunately, this is not so simple because the processes in small systems with lengths of the order of a few nm occur much faster than microscopic ones. A simple example is to compare the self-diffusion time τ between atoms and molecules; this is the time it takes for an isolated sphere of radius a to diffuse in a medium at a distance comparable to its radius:

$$\tau = \frac{a^2}{6D} \tag{2.20}$$

In the equation above, D is the diffusion coefficient. Molecules' self-diffusion time is in the order of picoseconds, while for colloidal particles (typically in the micrometric scale) is in the order of seconds. Hence, experimentally it is more convenient to study generic phenomena common to both systems, like crystallization or sedimentation, with colloids rather than molecules.

Apart from the time scale, we also have to consider the length scale. While atoms have a nanometric scale, colloids are on a micrometric scale, which allows us to extract direct information on individual particles' positions

with a conventional optical microscope. The scale of colloidal particles and their light scattering properties makes possible to manipulate them with optical tweezers, a very effective tool I have used in this thesis. Optical tweezers allow the manipulation of individual particles in a non-destructive way and help configure, transport, and arrange multiple particles easily.

Chapter 3

Fundamentals of Optical Tweezers

The first experimental realization of an optical tweezer was done by Arthur Ashkin (1922 - 2020) at Bell laboratories in the 1970s [32]. With a highly focused laser beam, he could trap latex particles of different micrometric sizes, which led to the development of an important tool widely used in science nowadays. With the help of optical tweezers, one can easily manipulate neutral microscopic bodies (and also neutral atoms [33]) with high precision without damaging the environment or the sample. Optical tweezers are widely operated in different research areas with an emphasis on biophysics, where they have been used to measure the rigidity of molecules [34] and explore the mechanical properties of DNA [35–38]. Other areas of interest where they are relevant are, for example, lab-on-a-chip devices [39], Brownian motion [40, 41], or particle alignment and sorting [42–44]. Combining a single laser beam with different optical elements, like Acousto-Optic Deflectors (AOD) or Spatial Light Modulators (SLM), offers the possibility to create multiple effective optical tweezers and complex potential landscapes to investigate more complicated scenarios [45–48].

The working principle of optical tweezers is based on the momentum exchange of light with a refractive medium. A light beam carries a momentum

$p = h\nu/c$, so when it interacts with a particle with a higher refractive index than its surrounding medium, its refraction creates an attractive potential well [49]. Since the photons produced by a laser are coherent (they have the same phase, frequency, and polarization state), they carry the same momentum, which creates the necessary force balance to generate the trapping. When the photons reach a dielectric particle suspended in a medium, the particle surface scatters the incident photons. Due to the different refractive indices of the particle and the medium, the photons are refracted inside the particle, changing their momentum. This change produces a reaction force on the particle.

We now analyze the interaction between the laser beam and the particle using ray optics analysis. Fig. 3.1 shows a schematic of the momentum exchange between the photons and the particle. There, we depict two situations: when the particle and the laser focus are in the same z plane but different x plane and the opposite situation. In the first case (Fig. 3.1 (a)), the particle experiences a net force towards the focus position. This force arises from the difference in the change of the light momentum in distinct regions of the particle due to the spatial light gradient. The particle region closer to the laser focus refracts more light than that farther, so the momentum change that originates due to the refraction of this region is higher, which induces a net force towards the laser focus. The resulting net force is called gradient force.

In the second case (Fig. 3.1 (b) and (c)), the particle and the laser beam focus are in different z planes. In this circumstance, there are two possibilities: the particle is in a z plane above the focus or below. When the particle is above the focal point (case c), the refraction of the incoming photons produces a momentum change along the upward direction. Hence, the resulting net force on the particle is downwards, dragging the particle towards the laser beam focus. The opposite happens when the particle is below the position of the focus. The net force of the momentum exchange pushes the particle upwards along the focus direction. The forces depicted in these two situations are the scattering force.

Note that the gradient force in Fig. 3.1 (a) also has a positive z component due to a scattering force component. Hence, the stable point of an optical

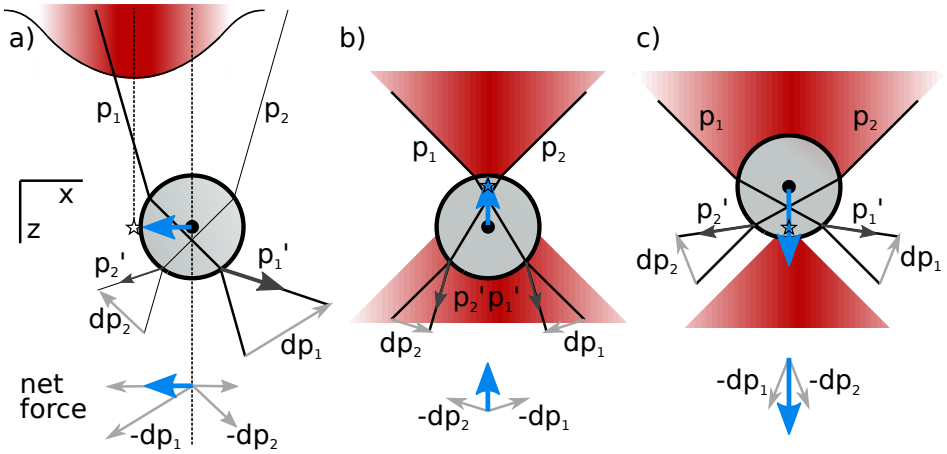

Figure 3.1: Schematics of the net force acting on a particle for different situations depending on the relative positions between the particle center and the laser focus. The red color gradient corresponds to the spatial light gradient, the star indicates the position of the focus, and the blue arrow is the net force exerted by the laser on the particle. a) the particle and the laser focus are in different x planes (gradient force origin), b) and c) the laser focus and particle center have different z positions (scattering force origin).

tweezer is not in the laser focal point but when the laser beam focuses slightly above the center of the particle. In this last situation, the upward force acting on the particle is compensated by the pushing scattering force produced by the partial reflection of the incident light plus the gravitational force, achieving stable trapping.

It is essential to have a strong gradient force to obtain stable optical tweezers. In practice, we can realize this situation with the help of an objective with a high numeric aperture (NA). Such an objective provides a sharp focus of the laser beam, so the spatial light gradient acquires a high steep. This way, the gradient force overcomes the scattering force, and we can confine the colloidal particle. In these conditions, the light gradient

produces a restoring force towards the equilibrium position responsible for particle confinement. The resulting force acts as a Hookean spring with a stiffness proportional to the light intensity [50].

3.1 The Acousto-Optic Deflector

I describe the basis of an Acousto-Optic Deflector (AOD), a device I used in the laboratory to create multiple optical traps. The working principle of an AOD is the change in the refractive index when an acoustic wave propagates in a material. The acoustic wave creates regions where the medium gets compressed in a periodic pattern according to the wave propagation. In these regions, the density and the refractive index are higher than those found where the medium is rarefied. In solids, the acoustic wave produces vibrations, which alters the polarizability of molecules and, thus, the refractive index changes [51].

This way, the acoustic wave creates stratified parallel planes with different refractive indices. The wavelength of sound Λ determines the separation between these planes, which partially reflect the light beam only if the incidence angle θ fulfills the Bragg condition for constructive interference [51]:

$$sin\theta = \frac{\lambda}{2\Lambda} \tag{3.1}$$

Where λ is the wavelength of light in the medium. This phenomenon is the Bragg diffraction, and the devices that implement it are known as Bragg cells (Fig. 3.2).

Fig. 3.2 shows a scheme of a Bragg cell where the incident beam of light is directly transmitted and partially diffracted within the cell. The directly transmitted light beam is called the zero order of the Bragg cell. The first order is the diffracted light beam generated by the interaction with the acoustic wave. Thus, the zero-order will always appear, whereas the first order only appears by interaction with an acoustic wave.

In practice, the AOD uses a radio frequency signal to create acoustic waves in a crystal that composes the Bragg cell. The modulation of the

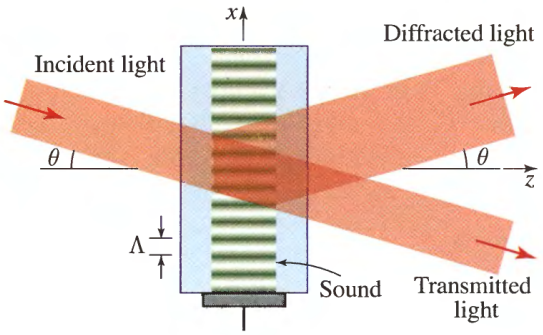

Figure 3.2: Schematic of a Bragg cell with the different parameters: Λ is the acoustic wavelength, θ is the incidence angle (in the scheme coincides with the diffracted angle, but it may not necessarily occur), and the directions of the incident, the transmitted, and the diffracted light beams. [51].

diffracted light beam angle depends on the input radio frequency signal, which allows the modification of the output laser direction. The advantage of the Bragg cells is that the diffraction pattern can change very fast with radio frequency signaling, so the diffracted beam can change its output angle in a very short time-lapse of the order of kHz. The typical self-diffusion time of suspended micrometric particles is of the order of seconds. Thus, as the laser beam visits different positions in a much shorter time-lapse, the created optical traps can be considered quasi-static or simultaneous. This property allows us to generate multiple optical tweezers for trapping colloidal particles.

Chapter 4

Methodology

In this chapter, I will present the methods, equipment, and software I used in the present thesis. I developed the experimental work of Chapters 5, 6, and 7 by using optical tweezers, which offer high versatility in manipulating microscopic particles and generating potential landscapes. I obtained the positions of the colloidal particles with optical microscopy techniques, which I analyzed using specific-developed software.

4.1 Optical Tweezers

Optical tweezers have played a central role in the realization of the different experiments, allowing us to achieve the trapping of microscopic particles with high precision. To create the optical tweezers, I used an infrared laser Manlight ML5-CW-P/TKS-OTS shown in Fig. 4.1 (a), which operates at a power of 6A/3W to create a continuous wave laser of wavelength $\lambda = 1064\mu$m. As shown in Fig. 4.2 (a), I deflect the laser source through an AOD AA Optoelectronics DTSXY-400-1064 (Fig. 4.2 (2)). The deflection of the AOD produces a trap at a position roughly proportional to the input frequency. As a trapping microscope objective, I use a 40x magnification Nikon water immersion objective operating dry (Fig. 4.2 (7)), which conjugates the AOD deflection plane to the focal plane. I use a two-channel radio frequency wave

generator DDSPA2X-D431b-34 (Fig. 4.1 (b)) to produce the input frequency of the AOD, which ranges from 60 to 90 MHz. To control the wave generator, I use a digital output card of National Instruments cDAQ NI-9403 (Fig. 4.1 (c)) with a refresh frequency of 150 kHz. This card introduces a value to the wave generator at a frequency of 50 kHz; hence the AOD can deflect the laser beam to a different position every 20 μs. Thus, I can create a series of effectively simultaneous optical traps because the time interval in which the laser visits a trap position is shorter than the typical self-diffusion time of the colloidal particles, which is $\tau \sim 10$s for polystyrene particles with 2 μm radius.

The optical path the laser beam follows is shown in Fig. 4.2 (a), where I have highlighted the main optical components used to realize the optical tweezers. In this picture, we find the collimator lens (Fig. 4.2 (3)), which in combination with the convergent lens (Fig. 4.2 (8)), modifies the aspect ratio of the incident laser beam. With this arrangement and the microscope objective (Fig. 4.2 (7)), I can reduce and focalize the laser beam such that it traps the microscopic colloidal particles.

When the beam enters the instrument, the AOD deflects the laser beam to the zero-order mode, so it deviates from the main optical path. Hence, I neglect this mode and only keep the first-order deflections produced by an RF input signal, which follows the main optical path depicted in Figs. 4.2 (a), (b), and (c).

It is also worth mentioning the role of the power meter in this setup (Fig. 4.2 (4) is the optical sensor, and Fig. 4.2 (5) is the power meter station), which I used to control the amplitude of the generated potential landscapes in the sample. I used LabView software to program a feedback loop system with which I modified the input voltage to the AOD and, thus, the strength of the optical tweezer in the colloidal suspension, depending on the measured optical power. This way, I minimized the laser power fluctuations, increasing the stability of the optical tweezer acting over the sample.

The optical path pases through a custom-built inverted optical microscope equipped with a second observation objective (Nikon 40x plan apo) inside a magnetic coil system in Fig. 4.2 b, which also serves as a sample holder. Finally, the optical path is closed by a CMOS camera (Ximea MQ003MG-

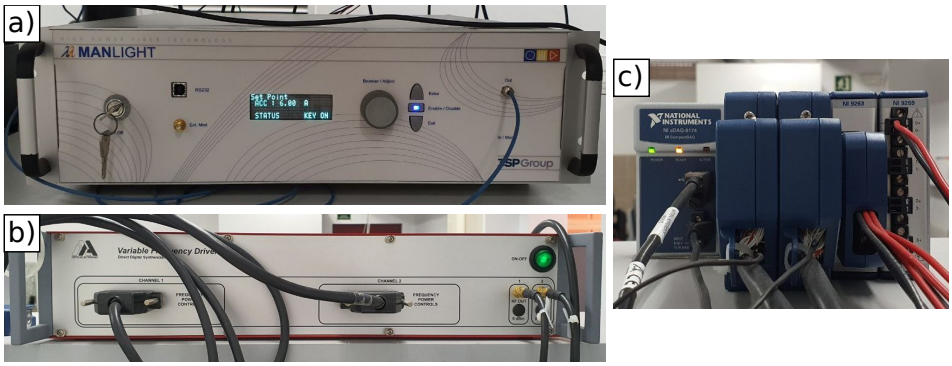

Figure 4.1: Images of the instruments used in the laboratory to generate the fast scanning optical tweezers: a) infrared laser generator Manlight ML5-CW-P/TKS-OTS, b) radio frequency wave generator DDSPA2X-D431b-34, and c) digital output card cDAQ NI-9403 from National Instruments.

CM, Fig. 4.2 10), which allows us to record videos at a framerate of up to 200 fps. We place an infrared filter (ThorLabs short pass filter, 850 nm cutoff) before the CMOS camera (Fig. 4.2 11) to avoid the interference of the optical tweezers in the resulting recorded video.

Fig. 4.3 shows a diagram of the optical path, where all the elements of the optic table have the same labels as Fig. 4.2. In this figure, I indicate the cut of the laser path after the beam splitters and the blocking of the zero-order deflected by the AOD. Also, one can easily see the position and role of the different lenses more clearly. Lenses L1 and L3 establish a simple lens system to expand the laser beam, while L2 is a convergent lens that converges the laser into the photodiode power detector.

4.1.1 Calibration of the Optical Tweezers

In the experimental setup, the optical tweezers focalize from above with a 40x Nikon objective, as shown in Fig. 4.2 (b). Hence, the position of this objective determines the focal point of the optical tweezers in the sample. To determine the focal point of the optical tweezer, I follow a proceeding to determine the best performance to confine the colloidal particles. I perform this calibration process before starting the set of measurements exposed in Chapters 5, 6, and 7 to achieve the best conditions for the potential landscape.

I dispose of a set of optical tweezers resembling the target experimental conditions, forming a ring with the number of optical traps I will use afterward. Then, I fill the optical ring by placing one colloidal particle in each optical trap. I record a video, registering the particle tracking simultaneously, of the particles' Brownian motion inside the potential wells created by the optical tweezers. Using a Python script, I calculate the average mean squared displacement performed by the ensemble of particles during one minute. After this minute, I modify the height position of the objective with a micrometer, taking the average mean squared displacement information for each new situation. Comparing the results, I find the minimum value of the particles' mean squared displacement, which indicates the maximum confinement for the considered optical beam intensity and, thus, the optimal position of the objective.

This process is essential to find the best objective position before starting a new set of measurements. The variable thickness of the cover-slips I use to create the fluid cell alters the relative distance of the colloidal particles to the objective, so the best-focusing position varies for each sample.

4.2 Realization of the Experimental Cell

The used colloidal system consists of a suspension of polystyrene particles in water with 4 μm diameter (CML Molecular Probes). The samples are closed fluid cells transparent to light to facilitate the observation in the optical microscope. I constructed these samples with two cover-slips that keep a

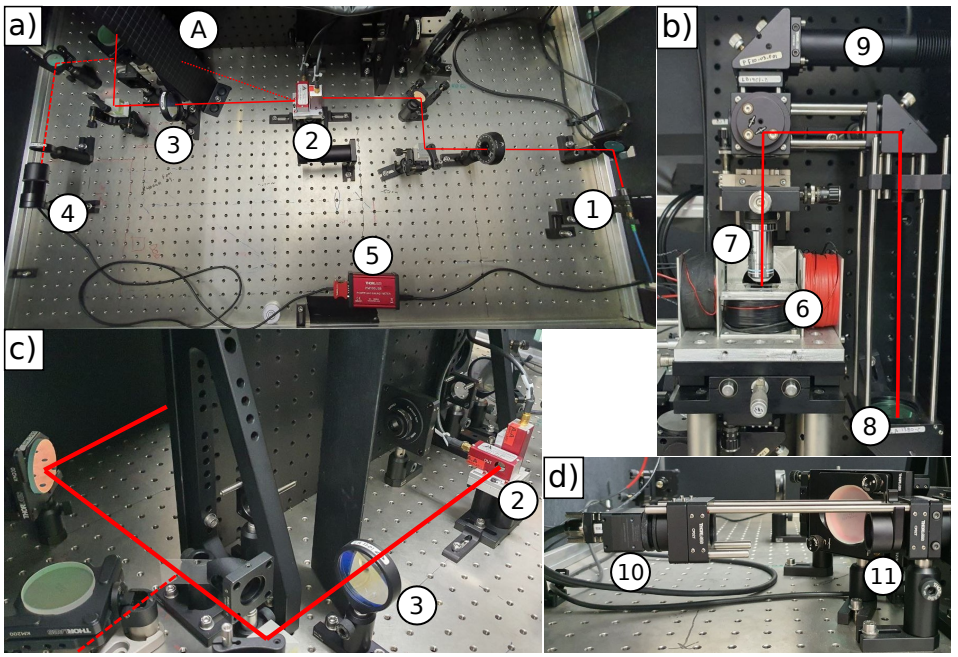

Figure 4.2: Image showing the optical path of the laser beam. The optical path is represented with the solid red line in (a), (b), and (c), while the dashed red line represents the path that part of the laser, deflected by the beam splitter, undergoes towards the power meter. The dotted line represents the zero-order of the AOD, whose path ends in the metallic screen (A). a) The laser path with the different optical components. The numbers indicate: (1) the laser beam entry, (2) the AOD, (3) the collimating lens, (4) the power meter sensor, and (5) the power meter. b) custom-made inverted optical microscope, with the incoming laser path represented by the solid red line, highlighting its main components: (6) the sample holder containing the observation objective 40x Nikon and the magnetic coil system used to apply external fields when needed, (7) the microscope objective 40x Nikon responsible of focalizing the laser beam and the light source, (8) is the convergent lens, and (9) is the LED illumination system. c) Image showing the detail of the final part of the optical path before entering the microscope. d) The CMOS camera Ximea MQ003MG-CM (10) and the infrared filter (ThorLabs short pass filter, 850 nm cutoff) (11).

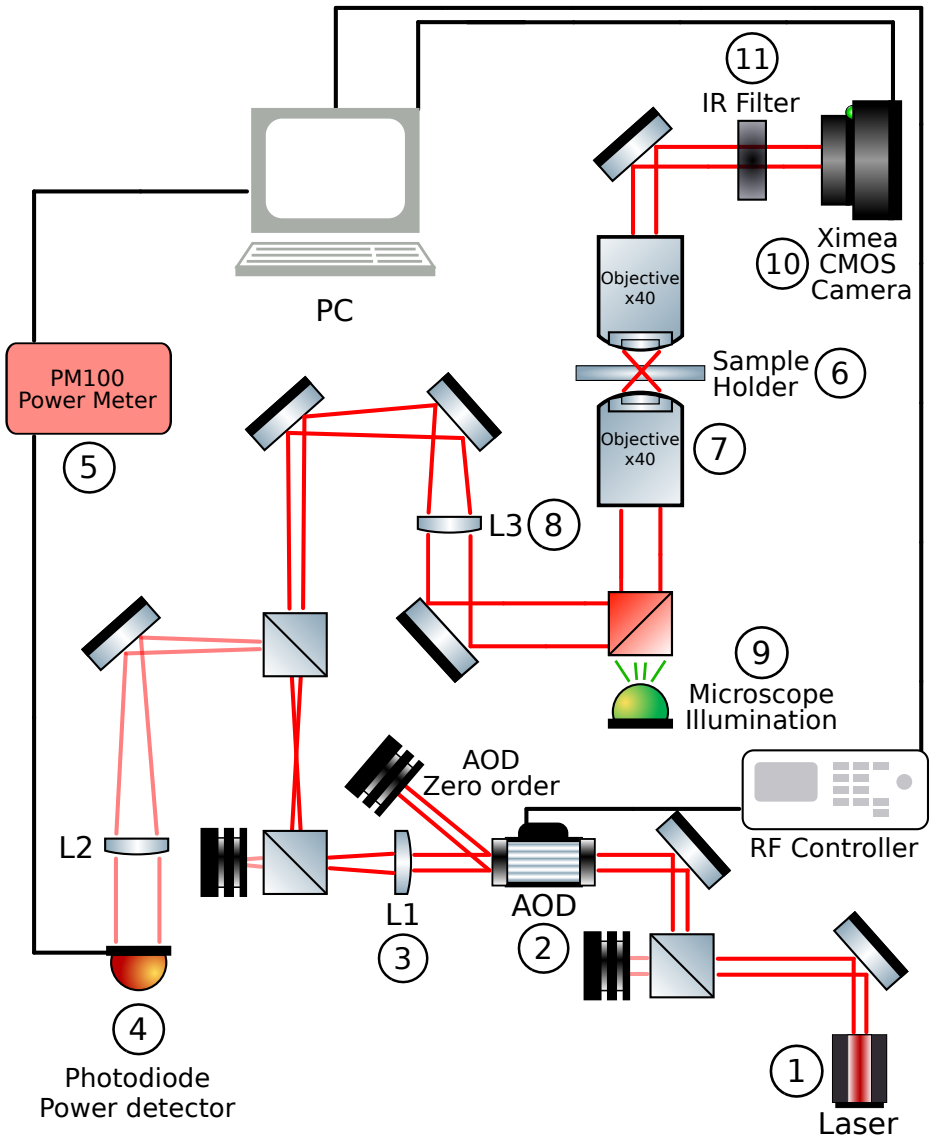

Figure 4.3: Diagram that reproduces the optical path followed by the laser beam with the different optical components. The relevant elements have the same labels as in Fig. 4.2. The lenses L1 and L3 compose a simple telescope to expand the laser beam. The lens L2 is necessary to converge the laser into the photodiode power detector (4). I extracted the components of the diagram from Ref. [52].

water solution of the polystyrene particles sealed with parafilm and vacuum grease. I adjusted the density of particles in water depending on the specific experiment to realize. In particular, I dispense between 2 and 10 μL of the CML batch suspension in 1 mL of MiliQ water.

To realize the cell, I used the following procedure. I cleaned two cover-slips with MiliQ water, acetone, and isopropanol. One of the cover-slips had a rectangular shape (50 $\times$ 24 mm), which will be the bottom of the cell, and the other was smaller with a squared shape (20 $\times$ 20 mm). Once cleaned, I placed two slips of parafilm along the bottom cover-slip and closed the fluid cell chamber with the other. I used a hot plate at 140 °C to melt the parafilm so that the two cover-slips glued together. Then, I introduce a droplet of the previously prepared solution containing the polystyrene particles in the cell. I removed the remaining solution outside the fluid cell with a tissue and sealed it using silicon-based vacuum grease placed around the borders of the upper cover-slip.

4.3 Software Analysis Tools

The principal source of data extracted from the experiments were video-recorded images with the help of a XIMEA complementary metal-oxide-semiconductor (CMOS) camera. Hence, I developed scripts based on Python [53] to extract the particle position from these videos. I also used these libraries to process the experimental data and obtain graphs. I obtained the individual particle trajectories with the tracking library trackpy [54] based on the Crocker-Grier algorithm [55]. This algorithm finds the center of the particles by computing the brightness-weighted centroid of each particle in the image, which determines the particle positions with sub-pixel resolution.

Chapter 5

Transport in Flow-Driven Systems

Particle transport on the microscale has become a trend of interest due to the large fields of application in science and technology. Some examples include applications in micro- and nanofluidic devices [56–58], the driven motion of particles through narrow channels [59–61], or in pores of zeolites [62], and through carbon nanotubes [63]. All these applications require a detailed understanding of the mechanisms involved in particle transport.

Collective transport of microscopic particles in fluid media can occur either due to external forces or to the drag produced by the movement of the surrounding fluid. Hence, the presence of the fluid implies the emergence of Hydrodynamic Interactions (HI) between neighboring particles. However, we find few reports studying the influence of these interactions on the collective transport behavior [64–70]. Even so, most of these investigations have focused on systems driven by external forces where they reported how HI enhance particle motion. For example, Ref. [47] describes the relevance of HI in facilitating surmounting potential barriers when particles are force-driven across an optical sawtooth potential.

In this section, we explore the scenario where particle transport is flow-driven, showing that the slowing down of the collective transport through

periodic potentials is a consequence of the HI between neighboring particles. We use a combined experimental and theoretical approach to show that HI can provoke an effective enhancement of potential barriers, causing jamming in transport at high particle density. This work, and that of the following chapters, has been developed in collaboration with the group of Prof. Philipp Maas at Osnabrük University, who have developed the numerical simulations.

5.1 Experimental Conditions

The experimental realization of a well-controlled flow-driven system is not a simple task since it has to overcome several difficulties to obtain suitable conditions. For example, the pressure field should be precisely controllable, and one should be able to vary the number of particles and the height of the potential barriers to explore the system under different conditions. Lithographically designed chambers are usually employed to analyze flow-driven transport, where the flow is produced by connecting a microfluidic channel to two-particle reservoirs at different pressures. However, when studying many-particle dynamics, such arrangement can originate undesired effects. For example, it can be difficult to precisely control the number of particles in the channel or even induce strong channel-reservoir coupling effects, which can influence particle dynamics. These couplings can lead to nonequilibrium steady states, causing the particle number density to become dependent on uncontrollable details [71].

To avoid such problems, we confined the colloidal particles in an optical ring of simultaneous potential wells (created by multiple optical tweezers) and characterized thus by periodic boundary conditions. Then, we generate a flow by rotating the optical potential to drive particles inside the circular landscape. Changing the reference frame to one co-rotating with the optically generated potential landscape, we find that the particle transport is equivalent to a situation of a flow-driven system.

In Fig. 5.1, I show a microscope image of the experimental system with a superposed plot of the generated potential landscape, which we create by placing $N_{tr} = 27$ optical traps along a ring of radius $R = 20.22$ μm. We

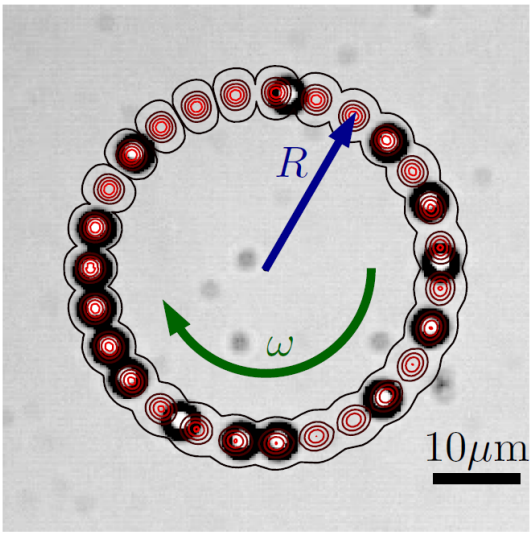

Figure 5.1: Optical microscope image showing the colloidal particles in the potential landscape generated by the optical tweezers. The superimposed scheme indicates the potential landscape shape and the depth of the potential wells. Arrows indicate the radius of the optical tweezer's ring and the direction of the motion. The scale bar is 10 μm.

choose the radius and the number of traps of the ring so that we obtain a separation between the traps comparable to the diameter of the colloidal particles, which is $2a = 4\mu$m. Hence, the distance between neighboring particles determines the wavelength of the periodic potential landscape $\lambda = 2\pi R/N_{nt} \simeq 4.7$ μm.

5.1.1 Realization of the Optical Landscape

Fig. 5.1 shows the obtained potential landscape $U(r)$, which confines the particles to a ring with potential wells at the center of each trap. We now consider the potential in polar coordinates $U(r, \varphi)$. The trap positions

determine a deep minimum along the radial direction at $r = R$, and N_{tr} pronounced minima along the azimuthal axis, represented with red lines in Fig. 5.1. The trap positions are rotated by changing the phase of the circulating beam linearly in time, moving at a constant velocity of $\omega = 0.63$ rad $\mathrm{s}^{-1} \simeq 6$ rpm, so the potential becomes time-dependent, $U = U(r, \varphi - \omega t)$. From now on, we analyze the system from the co-rotating reference frame where the trap positions are stationary: $\varphi \to \varphi - \omega t$. Besides, experimental observations indicate that the particles inside the optical ring exhibit negligible radial displacements, and thus we can consider the potential as one-dimensional $U_\varphi(\varphi) = U(R, \varphi)$.

We expect that the generated potential is periodic along the azimuthal direction with a period $2\pi/N_{tr}$. To check the validity of this hypothesis, I measured the optical forces by dragging a single particle along the ring and analyzing the displacements between successive frames, similarly to in Ref. [72]. Such method consists on analyzing the velocity of a particle inside the potential landscape. As the particle's velocity is given by the fluid drag and altered by the optical forces (Eq. (5.1)), we can extract the generated potential landscape by integrating the resulting expression after isolating the optical force contribution.

$$v(x) = v_{drag} + \frac{F_{opt}(x)}{\gamma} \tag{5.1}$$

Then, we only need to extract information about the particle velocity to obtain detailed information regarding the actual generated potential landscape. We show the result of this analysis in Fig. 5.2 (a), which reveals a non-perfectly λ-periodic experimental potential. The imperfections of the potential landscape are a consequence of the non-uniform response of the AOD, which makes the optical strength dependent on the deflected angle and, thus, a variation on the potential well depth with φ. The result is a static modulation of the potential amplitude with a relative strength ξ. With all these considerations, we reformulate the potential landscape by adding a periodic time dependence in its amplitude modulation, leading to

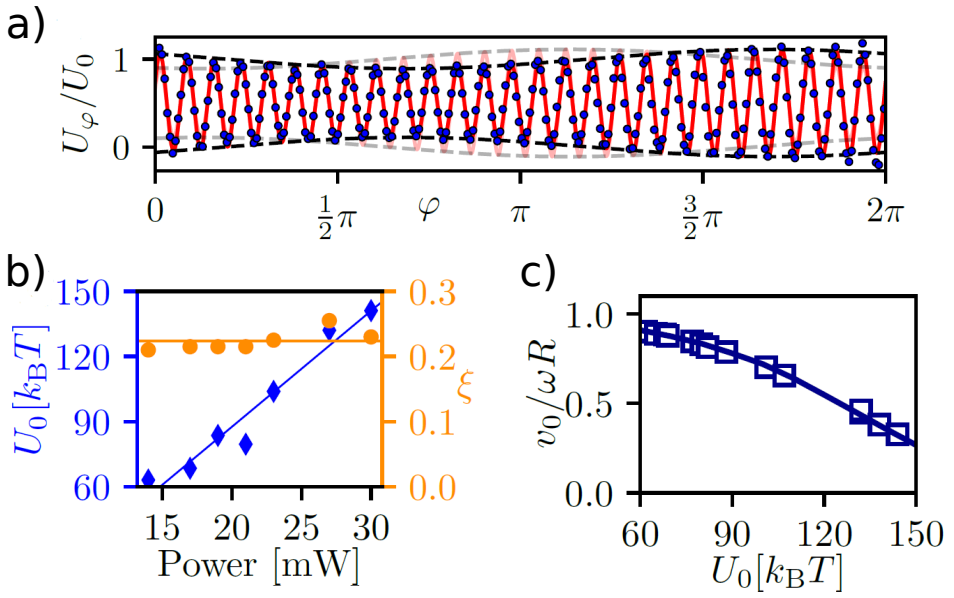

Figure 5.2: Experimental characterization of the optical landscape. a) Potential $U_\varphi(\varphi, t_0)$ as a function of φ. The faded line shows the potential at a later instant $t_0 + \Delta t$, and the dashed black lines indicate the potential amplitude modulation. We determine the experimental data (markers) by averaging the position increments of a single particle measured at a sequence of times $t_n = t_0 + 2\pi n/\omega$, $n = 0, 1, 2, \ldots$ b) Mean barrier height U_0 and modulation parameter ξ as a function of the laser power. c) Average single-particle velocity v_0 normalized to the flow velocity ωR as a function of the mean barrier height U_0. We compare the experimental values (symbols) to simulations (line) for the potential in Eq. (5.2).

$$U_\varphi(\varphi, t) = \frac{U_0}{2}\left[1 + \xi \sin(\varphi + \omega t)\right] \cos(N_{tr}\varphi) \tag{5.2}$$

We extracted the parameters of Eq. (5.2) by fitting the forces for various

laser powers in the range of 11 to 40 mW. Fig. 5.2 (a) shows the resulting filling to the experimental data, where the dashed line represents the modulation caused by the response of the AOD. We determined that the modulation strength is almost constant and independent of the laser power, $\xi = 0.22 \pm 0.02$. Moreover, we found that the mean barrier height U_0 between neighboring traps increases linearly with the laser power from 70 to 150 k_BT, where k_BT is the thermal energy. We show both trends in the plot of Fig. 5.2.

The Brownian dynamics simulations help to check the validity of the experimentally extracted parameters U_0, ξ, and D_0. The resemblance of the drag velocities v_0 obtained in simulations and experiments is the key to validating the applicability of the simulated results. The results in Fig. 5.2 (c) show an excellent agreement, signature of good reproducibility of the experimental conditions with the simulation parameters.

5.2 Dynamics of the Multi-Particle System

To characterize the collective many-particle dynamics, we measure the fundamental diagram [73], which is the relation between the particle current J and the particle density ρ.

To determine the current, I must first know the mean particle velocity. From the recorded videos obtained from the experiments, I extract the speed of individual particles from the position change between successive frames ($\sim$0.3 s) along the azimuthal direction. Then, I average the velocity of particles over time and the particle ensemble. Finally, I obtain the particle current $J = \rho \langle v \rangle / (2\pi R)$ with the obtained average velocity $\langle v \rangle$. I take the density of particles ρ as the fraction of potential wells occupied by the particles $\rho = N/N_{tr}$.

Fig. 5.3 (a) shows the experimentally measured current $J(\rho)$ for various barrier heights U_0. I normalize the particle current to that of the single particle $J_{sp} = v_0/(2\pi R)$, so we can easily compare the behavior for the different explored situations. If particles were independent without any interaction among them, the average velocity of particles would be equal

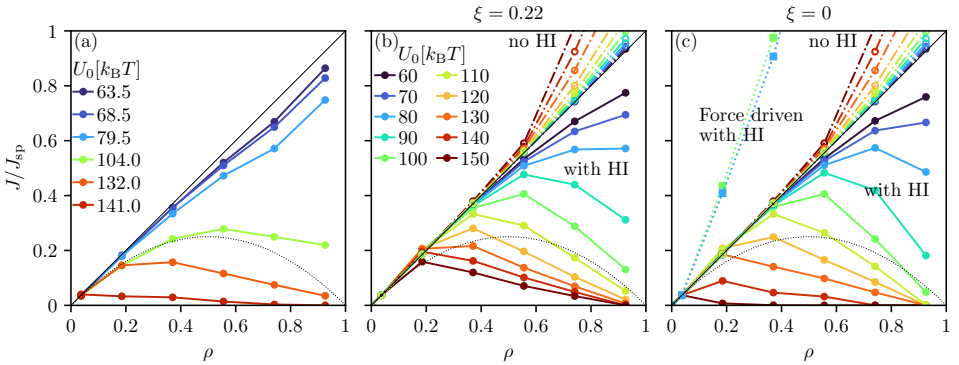

Figure 5.3: Fundamental diagrams for a) experiments and b), c) for simulations based on Eqs. 5.3. The current $J(\rho)$ is normalized with respect to the single-particle current $J_{sp} = v_0/(2\pi R)$, where v_0 is the single-particle velocity of Fig. 5.2 (c). Filled circles/solid lines and open circles/dashed-dotted lines refer to simulations with and without HI, respectively. In b), we show results for the time-dependent potential of Eq. 5.2 with amplitude modulation ($\xi = 0.22$). In c), we show the results for the ideal periodic potential ($\xi = 0$) and a force-drive system (squares/dotted lines). The legend in b) also applies to c). In all the graphs the solid black lines mark the behavior for independent particles, and the thin dotted line indicates the function $\rho(1-\rho)$.

to that of a single particle. I indicate this situation in the plot with the straight black line representing the linear function $J(\rho)/J_{sp} = \rho$. One can observe that the experimental results differ from the non-interacting particle scenario, which is only present in the limits of small particle density $\rho \to 0$. Therefore, the decrease of $J(\rho)/J_{sp}$ with increasing particle density reveals the emergence of interacting phenomena in the multi-particle system.

Moreover, the particle density is not the only cause for the current suppression, as one can also observe the current decreases with increasing barrier height, U_0. And not only the suppression of current is affected, but also the whole multi-particle behavior.

When $U_0 \lesssim 80 k_B T$, the particle current is close to the non-interacting

particle case with only a weak reduction from the linear trend. On the other hand, at higher barrier heights $U_0 \gtrsim 100 k_B T$, we observe a dramatic suppression of current. In these cases, the experimental data present a local maximum in $J(\rho)$, which displaces towards low ρ regions with increasing values of U_0. This behavior is a signature of jamming: a transition from fluid-like continuous motion to arrested states.

The Asymmetric Simple Exclusion Process (ASEP) [74, 75] provides a simple model describing the jamming behavior in driven systems. This theoretical model considers point-like particles in a squared periodic potential with asymmetric jumping probability to neighboring potential wells, forbidding jumps to previously occupied positions. This model predicts that the particle current obeys $J(\rho)/J_{sp} = \rho(1-\rho)$, which we represent in Fig. 5.3 with a black dotted line as a reference. However, the experimental results contrast with this simple model, revealing that the multi-particle dynamics are more complex, as suggested by the strong dependence on the potential barrier height U_0.

To understand the origin of the jamming, we performed Brownian dynamics simulations of hard-sphere interacting particles. The potential $U(\vec{r}_i)$ defines the optical forces acting on the particles at positions r_i, where $\vec{u}_i = \vec{\omega} \times \vec{r}_i$ are the azimuthal velocities of the particles ($\vec{\omega} = \omega \hat{z}$, where $\hat{z}$ is the unit vector in the z direction).

In the reference frame co-rotating with the optical traps, the translational motion of N particles in the presence of HI can be described by the Langevin equations [76]:

$$\dot{\vec{r}}_i = -\vec{\omega} \times \vec{r}_i + \sum_{j=1}^{N} \left[k_{\mathrm{B}} T \vec{\nabla}_j \vec{\mu}_{ij} + \vec{\mu}_{ij} \vec{f}_i \right] + \vec{\zeta}_i, \tag{5.3a}$$

$$\vec{f}_i = -\vec{\nabla}_i U(\vec{r}_i) + \vec{f}_i^{\,\mathrm{int}}\,, \tag{5.3b}$$

Where $\vec{f}_i^{\,\mathrm{int}}$ is the interaction force exerted on particle i by the other particles, and $\vec{\mu}_{ij} = \vec{\mu}_{ij}(\vec{r}_1, \ldots, \vec{r}_N)$ is the mobility tensor, which accounts for HI by the mobility method [77]. The vector $\vec{\zeta}_i$ is the Gaussian white noise described in Section 2.1.

Equation (5.3a) shows that the proposed experimental conditions effectively correspond to a system of interacting particles driven by an external flow field: a flow-driven system. The $\vec{\omega} \times \vec{r}_i$ term corresponds to the driving mechanism, a radially symmetric vortex flow field that forces the movement of particles inside the potential landscape. One can also check this fact by averaging $U_\varphi(\varphi, t)$ from Eq. (5.2) over one period of rotation $2\pi R/\omega$. The result is a function time-independent and periodic in φ with period $2\pi/N_{tr}$. Hence, the resulting average force of the time-averaged potential along the azimuthal direction is zero. In other words, the average particle current is zero without a fluid flow.

In the numerical simulations, the HI develop from the point of view of the Rotne-Prager form, which I showed in Section 2.3.1. With this method, one can obtain the mobilities $\vec{\mu}_{ij}$ for the reflective fluid flows resulting from the coverslip underneath the colloidal particles and those induced by the movements of the neighboring particles. This treatment of HI simplifies the experimental conditions, as it neglects lubrication effects, possible translation-rotation couplings, and expansions of the mobilities beyond the Rotne-Prager form for particles coming close to each other. Despite the simplification, one can see in Figure 5.3 that this approximation suffices to describe the experimental system qualitatively. All simulations consider the reflective fluid flow and constrain the particle movement to the azimuthal direction. In the following, when I refer to simulations with and without HI, I mean the particle-particle HI calculated in full-three dimensional space.

Figure 5.3 (b) shows the simulated normalized current $J(\rho)/J_{sp}$ obtained for the potential in Eq. (5.2) with the amplitude modulation obtained in the experiments ($\xi = 0.22$). The open circles connected by the dashed-dotted lines refer to the simulations without HI. In contrast to a decrease in the particle current, they show an enhancement at larger particle densities. This scenario dramatically changes when we include the HI, represented by the filled circles connected by solid lines. Presently, the normalized current decreases at large ρ in qualitative agreement with the experiments, where the jamming-like behavior becomes stronger when increasing U_0. However, one can still appreciate divergences from the experimental results of Fig. 5.3, which we attribute to the limitations of the minimal model of the HI.

In order to elucidate the role of the amplitude modulation of the potential landscape in the emergence of jamming, additional simulations treat the ideal case of a time-independent potential ($\xi = 0$ in Eq. (5.2)). I present the results of this case in Fig. 5.3 (c), which are very similar to those in Fig. 5.3 (b). Again, without HI, the particle current overpasses that of independent particles, while the inclusion of HI leads to jamming with increasing values of U_0. Therefore, we can discard any relevant interference coming from the amplitude modulation.

To summarize, simulations show that HI highly influence the experimental system. When we exclude the HI, the particle transport exceeds the single-particle current, enhancing the total current in the optical ring. On the other hand, when we introduce HI, the particle current becomes smaller than that of independent particles and decreases with ρ at large densities, reflecting jamming. We can also discard that this effect originated from the amplitude modulation since the simulations with and without such modulation of the potential landscape show minor changes in the behavior of the particle current.

5.2.1 Effect of Hydrodynamic Interactions

We now focus on the role of HI in particle transport, which are responsible for jamming in the flow-driven system. To this end, we consider the equation of motion of a single particle in the potential given by Eq. (5.2),

$$\dot{\varphi} = -\frac{\mu_0}{R^2}\frac{\partial}{\partial\varphi}\left[\frac{\omega R^2}{\mu_0}\varphi + U_\varphi(\varphi,t)\right] + \zeta_\varphi \tag{5.4}$$

Where $\langle\zeta_\varphi(t)\zeta_\varphi(t')\rangle = 2D_0R^{-2}\delta(t-t')$ with $D_0 = k_BT\mu_0$, and μ_0 the mobility of the particle. Hence, $U_\varphi(\varphi,t)$ is tilted by the linear potential $\omega R^2\varphi/\mu_0$, resulting in the effective potential $U_\varphi^{eff}(\varphi,t) = U_\varphi(\varphi,t) + \omega R^2\varphi/\mu_0$. For small U_0, the tilting dominates the potential landscape, so the effective potential appears as if it had no barriers. Therefore, the flow drags a single particle, which finds little resistance to the movement. The part U_φ in U_φ^{eff} can be interpreted as creating resistance to the particle motion when

driven by the flow field. Therefore, it causes the single particle velocity v_0 to be smaller than the flow velocity ωR for $U_0 > 0$ and to decrease with U_0.

When U_0 becomes larger than a critical amplitude U_{0c}, the single-particle motion becomes thermally activated, and particle motion originates from the random Brownian forces. For determining U_{0c}, we take the temporally period-averaged potential $\bar{U}_\varphi^{eff}(\varphi) = (\omega/2\pi)\int_0^{2\pi/\omega} U_\varphi(\varphi, t)\,\mathrm{d}t$, which is also the effective potential for the ideal case of a time-independent potential ($\xi = 0$ in Eq. (5.2)). The barriers in $\bar{U}_\varphi^{eff}(\varphi)$ arise when U_0 becomes higher than the critical amplitude $U_{0c} = 2\omega R^2/(\mu_0 N_{tr}) \simeq 147 k_B T$.

For this reason, all experiments are below the critical amplitude, and therefore one would expect linear current-density relations with no pronounced jamming effect. Indeed, the simulation data without HI shown in Fig. 5.3 (b) confirms this prediction. However, the HI contributes to effectively increasing the potential barrier. In the absence of HI, we only consider the terms $j = i$ of Eq. (5.3a), meaning that the mobility of particles is not affected by external actors. However, this situation changes when the HI emerge. With the Rotne-Prager level of description, the external contributions to the particle mobility extend only to the particles j closest to particle i. Thus, the estimated contribution of a particle j located at a neighboring trap of a particle i is $\mu_0[3a/\lambda - 2a^3/\lambda^3]\partial U_\varphi/\partial\varphi$, being a the particle radius and λ the wavelength of the potential. Hence, leading to an effective enhancement of the mean barrier height U_0 by HI to a value:

$$U_0^{HI} = \left(1 + 3\frac{a}{\lambda} - 2\frac{a^3}{\lambda^3}\right) U_0 \tag{5.5}$$

Because $a < \lambda$, the additional contribution is always positive ($U_0^{HI} > U_0$). Using Eq. 5.5 with $\lambda = 2\pi R/N_{tr} \simeq 4.71\mu$m and $a \simeq 2\mu$m, U_0 is doubled. Thus, the effective potential barriers enhanced by the HI overcome the U_{0c} value at smaller U_0. Now, the potential landscape presents barriers where there were not without HI. This behavior also agrees with the current suppression at large ρ. When the occupancy of potential wells is higher, there are more probabilities of finding neighbors that strengthen the potential barriers, increasing the current suppression. Besides, we still must consider

the possible blocking effects derived from the particle density increase, leading to a further slowdown of particle dynamics [78, 79]. One can see in the experimental videos shreds of evidence of hopping motion and jamming phenomena, also collected by the measured trajectories in the cases of large U_0 and high densities.

5.3 Comparison with a Force-Driven System

Here, we compare the results obtained for a flow-driven system with a force-driven one. The motivation originates from the different behavior observed compared to other reports on force-driven systems [47].

To explore whether the jamming would occur in a force-driven system, we solved the Langevin equiations (5.3) for particles driven by the external torque $\vec{f}_{ext}(\hat{\varphi}) = -\omega R\hat{\varphi}$, where $\hat{\varphi}$ denotes the unit vector along the azimuthal direction; this means that Eq. (5.3a) becomes

$$\dot{\vec{r}}_i = \sum_j \left\{ k_B T \vec{\nabla}_j \vec{\mu}_{ij} + \vec{\mu}_{ij} \left[\vec{f}_i + \vec{f}_{ext}(\hat{\varphi}) \right] \right\} + \vec{\zeta}_i \tag{5.6}$$

If we compare the expressions (5.3a) and (5.6), we observe that the force position has changed from inside the sum to the outside. This change reflects the different mechanisms occurring in both systems. In Eq. (5.3a), we observe that the fluid vortex responsible for the particle driving is outside the sum term, whereas for the later expression derived for a force-driven system, we find the force contribution f_{ext} inside. Therefore, in the flow-driven case, the external force applies after considering all the modifiers to the mobility tensor, so it actuates over the whole particle ensemble. The opposite occurs for the force-driven system, which contemplates the contribution of the external force within the terms that affect the mobility tensor, so in this situation, the force acts over the particles individually.

Thus, as the external force acts differently in each case, we should expect that HI contribute distinctly. The fact that the modifiers of the mobility tensor apply to the driving force implies that the HI also influence the driving. Hence, in the force-driven system, we find that the enhancement

factor found in Section 5.2.1 applies not only to the potential barriers but also to the external driving. Implementing this reasoning to the experimental conditions, which develop under low noise conditions ($k_BT \ll U_0$), the HI effective contribution is a speed-up effect of all the particles. The opposite situation occurs in flow-driven systems, where HI enhancement only applies to the optical barriers and, hence, the overall effect is the reduction of the particle current.

We show the results of simulations performed in the force-driven case with the squares connected by dotted lines in Fig. 5.3 (c). In contrast to the flow-driven case, one can see that the particle transport experiences an intense current enhancement, in agreement with previous findings [64].

5.4 Conclusions

In this chapter, I have used colloids confined and driven by an optical ring to show that the flow behavior in flow-driven many-particle systems differs from previously reported results for force-driven systems. With my analyses, I could discern the differences between flow- and force-driven mechanisms, elucidating the effect of HI in both scenarios.

The experimental and simulated data display satisfactory qualitative agreement but not perfect quantitative. We could obtain better matching between experiments and simulations by refining the description beyond the Rotne-Prager approximation. Such modifications can include higher-order terms in the expansion of mobilities in powers of the particle radius to inter-particle distance ratio a/λ, lubrication effects, and additional consideration of the rotational dynamics of the particles.

Thus, the performed analysis provides an accurate theoretical description of the phenomenon occurring in the experiments. The described interaction mechanisms can also apply to diverse scenarios. Transport of matter over energic barriers in a fluid suspension is typical in many soft matter, biological systems, and microfluidic devices. Therefore, I expect the phenomena uncovered here will be of general importance for further studies and applications of flow-driven many-particle systems.

Chapter 6

Jamming in Flow-Driven Systems

In the previous chapter, I showed that HI induce jamming in a flow-driven system. In this chapter, I expand the analysis to explore the effect of different system parameters, like relative particle size, on the transport through HI. I also present a deeper analysis of the potential landscape shape and its characterization.

A wide variety of biological and soft matter systems are affected by HI [80]. For example, they influence the organization of sperm cells [81] and magnetotactic bacteria [82], modify the dynamics of bacteria propelling close to a surface [83–85], or they induce synchronizaztion phenomena [86–92]. Besides, there are also investigations about the effect of HI in the context of particle sedimentation [93–95], confinement [96–98], pattern formation [99, 100] or crystallization kinetics [101, 102]. For this reason, we investigate the role of HI between spherical particles. Our system provides a relatively simple model that allows us to explore the impact of HI on transport properties, circumventing problems derived from more complicated biological systems characterized by non-trivial shapes and interactions. Therefore, we expect that the results extracted from this analysis may provide relevant information applicable to other physical systems.

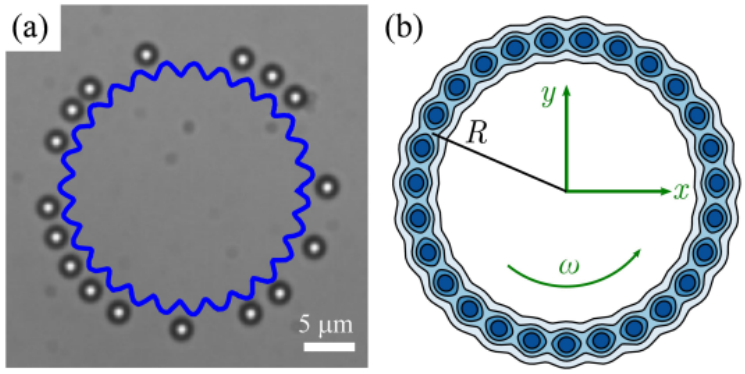

Figure 6.1: Experimental system. a) Optical microscope image showing $N = 17$ colloidal particles of radius $a = 2\mu$m trapped along a ring with $N_{tr} = 27$ equidistant optical traps (blue line). b) Isolines of the periodic potential generated by the scanning laser tweezers with angular velocity ω. The experiments are performed for different ring radii $R = 17.8\mu$m, 20.2μm, and 21.8μm.

6.1 Optical Potential Landscape

Fig. 6.1 shows a microscopic image of the experimental system considered here and the experimentally generated potential landscape.

The experimental system consists of $N_{tr} = 27$ time-shared optical tweezers evenly spaced along a ring of radius R. The ring confine colloidal particles of radius $a = 2\mu$m in the positions of the optical tweezers, which define the locations of the potential wells. The optical traps rotate with angular speed ω to induce a vortex flow, forcing the confined particles to move along the optical ring, jumping across the neighboring potential wells.

The distance between two neighboring potential wells determines the wavelength of the potential landscape, which is:

$$\lambda = \frac{2\pi R}{N_{tr}} \tag{6.1}$$

Then, one can relate the size of the colloidal particles with λ to obtain the relative particle size a/λ. This relation is practical to explore the dynamics of different particle sizes to the potential landscape features without changing the physical particle radius a. Hence, I modified the ring radius R while keeping N_{tr} constant to vary the relative particle size.

6.1.1 Theoretical description

One can describe the experimentally generated potential landscape, shown in Fig. 6.1 (b), created by the optical traps positioned at (x_{tr}, y_{tr}) with a Gaussian profile:

$$U_{tr}(x, y; x_{tr}, y_{tr}) = -u_0 \exp\left[-\frac{(x - x_{tr})^2}{2w^2} - \frac{(y - y_{tr})^2}{2w^2}\right] \tag{6.2}$$

Where $w = 2.02\mu$m is the width of a trap, and u_0 is its depth determined by the laser power. For describing the circular arrangement of the traps in Fig. 6.1, we use polar coordinates, where $(x, y) = (r\cos\varphi, r\sin\varphi)$ and the trap center positions are at $(x_{tr}, y_{tr}) = (R\cos\varphi_k, R\sin\varphi_k)$, $k = 1, \ldots, N_{tr}$ with $\varphi_k = 2\pi k/N_{tr}$, being R the ring radius.

Then, the sum of the contributions of each trap determines the static potential of the optical ring:

$$\begin{aligned} U^{st}(r, \varphi) &= \sum_{k=1}^{N_{tr}} U_{tr}(x, y; x_k, y_k) \\ &= -u_0 \sum_{k=1}^{N_{tr}} \exp\left[-\frac{r^2 + R^2 - 2rR\cos(\varphi - \varphi_k)}{2w^2}\right] \end{aligned} \tag{6.3}$$

Due to the intense radial confinement of the particles, displacements of the colloidal particles along the radial directions are almost negligible. Hence, we can set $r = R$ in Eq. (6.3), which leads to a potential landscape expression that depends only on the azimuthal angle φ:

$$U_\varphi^{st}(\varphi) = -u_0 \sum_{k=1}^{N_{tr}} \exp\left[-\frac{R^2}{w^2}(1-\cos(\varphi-\varphi_k))\right] \tag{6.4}$$

This potential has the period $2\pi/N_{tr}$, $U_\varphi^{st}(\varphi + 2\pi/N_{tr}) = U_\varphi^{st}(\varphi)$. Expanding it into a Fourier series, we obtain

$$U_\varphi^{st}(\varphi) = \sum_{n=-\infty}^{\infty} c_n \exp(iN_{tr}n\varphi) \tag{6.5}$$

where

$$\begin{aligned} c_n =& \frac{N_{tr}}{2\pi} \int_{-\pi/N_{tr}}^{\pi/N_{tr}} \mathrm{d}\varphi U_\varphi^{st}(\varphi) \exp(-iN_{tr}n\varphi) \\ \simeq& -u_0 \frac{N_{tr}}{2\pi} \int_{-\pi/N_{tr}}^{\pi/N_{tr}} \mathrm{d}\varphi \exp\left[-\frac{R^2}{w^2}(1-\cos\varphi)\right] \exp(-iN_{tr}n\varphi) \end{aligned} \tag{6.6}$$

To go from the first to the second line in Eq. (6.6), we have kept only the summand for $k = N_{tr}$ when inserting $U_\varphi^{st}(\varphi)$ from Eq. (6.4). We can do this because of the large ratio $(R^2/w^2) \simeq 100$ in the experiments, which means that the summands for $k \neq N_{tr}$ are negligible in the integration interval. Likewise, we can set $(1-\cos\varphi) \simeq \varphi^2/2$ in Eq. (6.6) and extend the limits of integration to $\pm\infty$. The resulting Gaussian integral gives

$$c_n \simeq -u_0 \frac{N_{tr}w}{\sqrt{2\pi}R} \exp\left[-\left(\frac{N_{tr}w}{R}\right)^2 \frac{n^2}{2}\right] \tag{6.7}$$

Since $(N_{tr}w/R)^2/2 \simeq 3.6$, the Fourier coefficients decay quickly. The ratio c_2/c_1 is already of the order 10^{-5}, which allows a truncation of the Fourier series after $n = 1$, leading to a sinusoidal form of

$$U_\varphi^{st}(\varphi) \simeq c_0 + \frac{U_0}{2}\cos(N_{tr}\varphi) \tag{6.8}$$

with potential barrier

$$U_0 = 4c_1 = -2u_0\sqrt{\frac{2}{\pi}}\frac{N_{tr}w}{R}\exp\left[-\frac{1}{2}\left(\frac{N_{tr}w}{R}\right)^2\right] \tag{6.9}$$

Ref. [103] gives a similar derivation of this result, while Ref. [72] reports a sinusoidal form of the experimental potential resulting from a periodic arrangement of Gaussian optical traps. For the radii R studied in our experiments, the relative deviation between $U_\varphi^{st}(\varphi)$ from Eq. (6.4) and the approximate sinusoidal potential of Eq. (6.8) is less than 0.15% for all φ.

The rotation of the traps along the ring with angular frequency ω leads to the time-dependent potential in the laboratory reference frame:

$$U_\varphi(\varphi, t) = U_\varphi^{st}(\varphi - \omega t) = c_0 + \frac{U_0}{2}\cos(N_{tr}(\varphi - \omega t)) \tag{6.10}$$

In a corotating reference frame, this traveling-wave type potential reduces to $U_\varphi^{st}(\varphi)$.

In experiments, we evaluate the potential by analyzing the single-particle dynamics. For the kinematic viscosity $v \simeq 10^{-6}m^2/s$ of water and azimuthal velocity ωR, the Reynolds number is $Re = \omega R\sigma \simeq 3\times10^{-5} \ll 1$.The velocity correlation time $(4\pi a^3\rho_{PS}/3)/(6\pi\rho_{H_2O}va) \simeq 1\mu$s for the polystyrene beads is much smaller than the characteristic diffusion time $a^2/D_0 \simeq 30$s (where ρ_{PS} and ρ_{H_2O} are the densities of polystyrene and water respectively). To obtain the value of D_0, I performed independent measurements of the time-dependent mean-square displacements in the absence of the optical force fields, which yielded to the diffusion coefficient $D_0 \simeq 0.1295\ \mu\text{m}^2\text{s}^{-1}$.

Under these conditions, inertia effects are negligible, and a single particle performs an overdamped Brownian motion described by the Langevin equation:

$$\frac{\mathrm{d}\vec{r}}{\mathrm{d}t} = -\mu_0\vec{\nabla}U_{opt}(\vec{r}, t) + \vec{\zeta}(t) \tag{6.11}$$

where $U_{opt}(\vec{r}, t)$ is the potential of the optical forces, μ_0 is the mobility, and $\vec{\zeta}(t)$ is the Gaussian white noise with $\langle\vec{\zeta}\rangle = 0$ and $\langle\zeta_\alpha(t)\zeta_\beta(t')\rangle = 2D_0\delta_{\alpha\beta}\delta(t-t')$; $D_0 = k_BT\mu_0$ is the diffusion coefficient.

As we only have to consider displacements in the azimuthal direction, Eq. (6.11) simplifies to:

$$\frac{\mathrm{d}\varphi}{\mathrm{d}t} = \frac{\mu_0}{R^2}\tau_{opt}(\varphi, t) + \zeta_\varphi \tag{6.12}$$

where $\langle\zeta_\varphi\rangle = 0$, $\langle\zeta_\varphi(t)\zeta_\varphi(t')\rangle = 2D_0R^{-2}\delta(t-t')$, and $\tau_{opt}(\varphi, t)$ is the torque excerted on the particle:

$$\tau_{opt}(\varphi, t) = -\frac{\partial U_\varphi(\varphi, t)}{\partial\varphi} \tag{6.13}$$

In the corrotating reference frame with the angle variable $\varphi' = \varphi - \omega t$, Eq. (6.12) becomes:

$$\frac{\mathrm{d}\varphi'}{\mathrm{d}t} = \frac{\mu_0}{R^2}\left[\frac{\omega R^2}{\mu_0} + \tau'_{opt}(\varphi')\right] + \zeta_\varphi \tag{6.14}$$

where $\tau'_{opt}(\varphi') = (N_{tr}U_0/2)\sin(N_{tr}\varphi')$ is a time-independent torque.

6.1.2 Characterization of the Experimental Conditions

Unfortunately, the experimental realization of the potential landscape differs from the ideal conditions discussed in the previous section. As one can see in Fig. 6.2 (b), the torque in the corotating reference frame is not perfectly sinusoidal, presenting a periodic time dependence $\tau'_{opt} = \tau'_{opt}(\varphi', t) = \tau'_{opt}\left(\varphi', t + \frac{2\pi}{\omega}\right)$.

To obtain the shape of the experimentally generated potential landscape, I placed a single particle on the ring and recorded its motion with a video for 30 min at a time resolution of 30 frames per second ($\delta t = 1/30$s) and extracted the two-dimensional particle trajectory. After conversion to polar coordinates, I obtain the time series of the azimuthal positions of the particle $\varphi(t)$ while obviating the radial positions $r(t)$ because of the intense radial confinement.

With the azimuthal position of the particles, I proceed to obtain the optical torque with a similar method to in Ref. [72]. From Eq. (5.1), after adapting it to the experimental features, we can reach the expression:

$$\tau'_{opt}(\varphi', t) = \frac{R^2}{\mu_0}\left[\frac{\varphi'(t+\delta t) - \varphi'(t)}{\delta t} - \omega\right] \tag{6.15}$$

Where $\varphi'(t)$ is the azimuthal position of the particle at time t, δt is the time interval between consecutive frames of the video, ω is the drag velocity given by the rotation speed of the ring, R is the ring radius, and μ_0 is the particle mobility, which I obtained through the relation $\mu_0 = D_0/k_BT$.

The periodicity of $\tau'_{opt}(\varphi', t)$ in the experimental system requires an increase of the resolution on the trajectory data to obtain better fitting results. To do so, I divide the trajectory into spatial and temporal bins to perform an average of all the data available for each bin. In the spatial case, I split the periodicity $[0, 2\pi]$ into $N_\varphi = 270$, so there are ten bins of width $\Delta\varphi' = 2\pi/N_\varphi$ for each wavelength of the optical potential. Likewise, I obtain $N_\omega = 15$ temporal bins in the interval $[0, 2\pi/\omega]$ of width $\Delta t = 2\pi/(\omega N_\omega)$. Then, the bin intervals are $\mathfrak{J}_j = [(j-1)\Delta\varphi', j\Delta\varphi']$, $j = 1, \ldots, N_\varphi$, and $\mathcal{K}_k = [(k-1)\Delta t, k\Delta t]$, $k = 1, \ldots, N_\omega$ and have the midpoints $\varphi'_j = (2j-1)\Delta\varphi'/2$ and $t_k = (2k-1)\Delta t$. Finally, I obtain $\tau'_{opt}(\varphi', t)$ with the expression:

$$\tau'_{\mathrm{opt}}(\varphi'_j, t_k) = \frac{R^2}{\mu_0}\left[\frac{\left\langle [\varphi'(t+\delta t) - \varphi'(t)] \,\middle|\, \varphi'(t) \in \mathfrak{J}_j,\, t \in \mathcal{K}_k \right\rangle}{\delta t} - \omega\right] \tag{6.16}$$

The brackets $\langle \ldots \rangle$ means an average over many times in the measurement under the condition that $\varphi'(t)$ is in the bin interval $\mathfrak{J}_j$ and the time t in the bin interval $\mathcal{K}_k$. When applying Eq. (6.16), the angle $\varphi = \varphi(t)$ and the time t are first mapped to the intervals $[0, 2\pi]$ and $[0, 2\pi/\omega]$.

I show an overview of the described process in Fig. 6.2. Fig. 6.2 (a) illustrates the particle tracking, and Fig. 6.2 (b) shows representative results for the torque at two different times in the corresponding frame, see the blue lines of the graph for $\tau'(\varphi_j, t_1)$ and $\tau'(\varphi_j, t_{10})$. There, one can see the deviation of the experimental data from the ideal traveling waveform, which one would expect to be a sinusoidal function for the torque in the corotating reference frame.

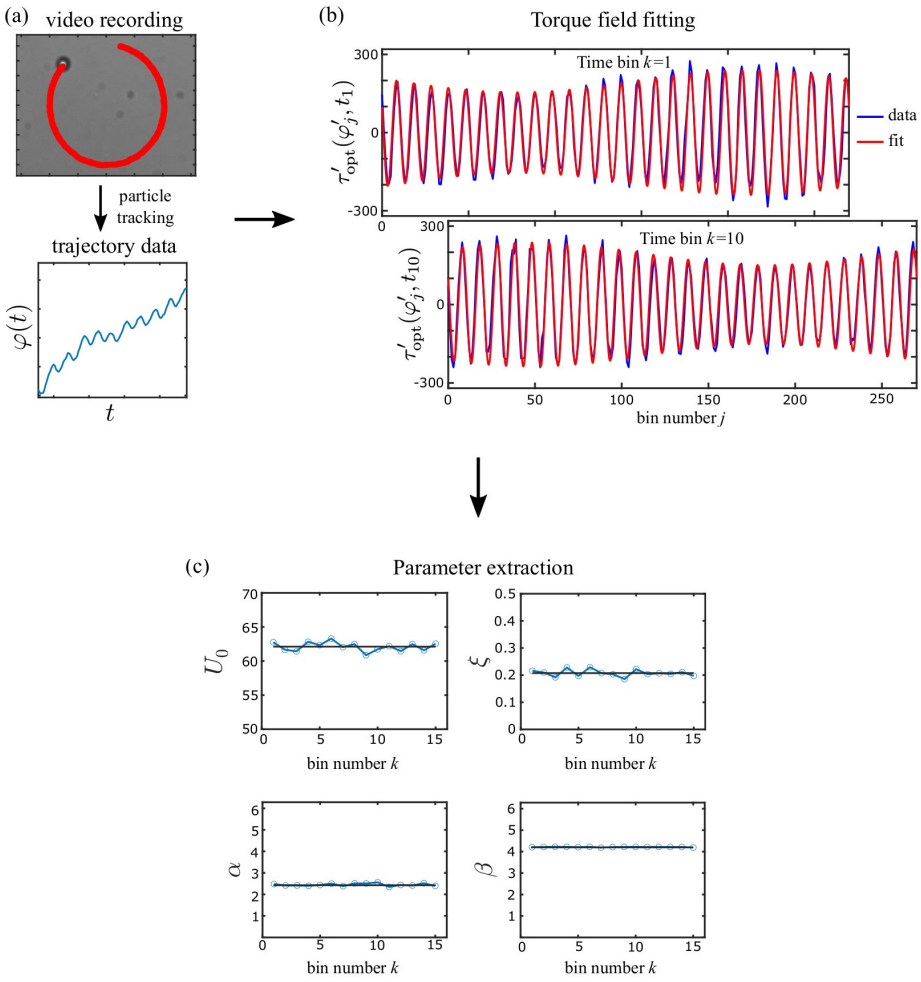

Figure 6.2: Method to determine the potential parameters from single-particle measurements. a) Illustration of the particle tracking. b) Fitting of the torque. The blue lines show representative results for the torque $\tau'_{opt}(\varphi', t)$ at two different times t_1 and t_{10} in the corotating frame obtained from measured trajectories using Eq. (6.16). The red lines are fits of Eq. (6.18) to the experimental data. c) Parameters U_0, ξ, α, and β extracted from the fitting.

Now, I provide a reformulation of the potential landscape in the corotating reference frame of Eq. (5.2), where the barrier height is modulated with a strength ξ, and U_0 thus represents a mean barrier height.

For comparison with the torque data in Fig. 6.2, we must consider phase shifts α and β for both the periodic trap arrangement and the amplitude modulation. Taking the time instant $t = 0$, the shift α accounts for the phase difference between the maxima of the $\cos(N_{tr}\varphi)$ function and an arbitrary but fixed zero point of φ along the ring in Fig. 6.1 (b). Likewise, the shift β accounts for the phase difference between the maximum of the barrier height modulation and the zero point. In the corotating reference frame, we then have:

$$U'_{\varphi}(\varphi', t) = \frac{U_0}{2}\left[1 + \xi \sin(\varphi' + \beta + \omega t)\right] \cos(N_{tr}(\varphi' + \alpha)) \tag{6.17}$$

and,

$$\begin{aligned}\tau'_{opt}(\varphi', t) =& \frac{U_0}{2}\Big\{\xi \cos(\varphi' + \beta + \omega t) \cos(N_{tr}(\varphi' + \alpha)) \\ &+ N_{tr}\left[1 + \xi \sin(\varphi' + \beta + \omega t)\right] \sin(N_{tr}(\varphi' + \alpha))\Big\}\end{aligned} \tag{6.18}$$

To determine the parameters U_0, ξ, α, and β, we fitted Eq. (6.18) to the experimental data for each time bin, Fig. 6.2 (c). For all the parameters above, we obtain constant values with minor numerical uncertainties, which proves that the functional form of Eq. (6.17) accurately represents the experimental optical potential.

We found that all the parameters agreed with the ones estimated from the experimental trajectories except U_0, which we underestimated by a few percent. The reason is that the time resolution in the experiment was not appropriate (δt a bit too large). Fig. 6.3 shows that the simulated v_0 (solid line) agrees well with the experimental data (symbols).

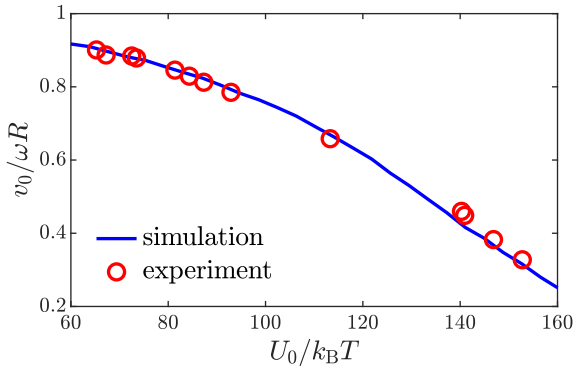

Figure 6.3: Comparison of measured (symbols) with simulated (line) mean velocity of a single particle as a function of the mean barrier height U_0 for ring radius $R = 20.2\mu$m, angular frequency $\omega = 0.63$rad/s of optical trap rotation, and potential amplitude modulation $\xi = 0.22$.

6.2 Equations of Motion for the Particle Dynamics

The Langevin equations in Eq. (5.3) describe the driven Brownian motion of the N colloidal particles. Adapting the expression to the coordinate change for the corotating reference frame, we have:

$$\dot{\vec{r}}_i' = -\vec{\omega} \times \vec{r}_i' + \sum_{j=1}^{N} \left[k_B T \vec{\nabla}_j' \vec{\mu}_{ij} - \vec{\mu}_{ij} \vec{\nabla}_j' U_{opt}'(\vec{r}_j', t) + \vec{\zeta}_i \right] \tag{6.19}$$

Here, the prime indicates that we are working with the corotating reference frame, so $\vec{\nabla}_i'$ takes the derivative to the primed coordinates, and $U_{opt}'(\vec{r}_i', t) = U_{opt}(\vec{r}_i - \vec{\omega} \times \vec{r}_i t, t)$.

With the expression for the mobility tensor given in Section 2.3.1, its divergence reduces to a simple derivative to the distance z of the particles from the coverslip surface. Due to the nature of the optical tweezers' confinement, we estimate that the particles are at a constant mean distance

from the coverslip surface. This estimation is reasonable as the optical tweezers confine the particles from above by pushing the colloidal particles against the coverslip surface. Hence, Eq. (6.19) reduces to:

$$\frac{\mathrm{d}\vec{r}_i'}{\mathrm{d}t} = -\vec{\omega} \times \vec{r}_i' - \sum_{j=1}^{N} \vec{\mu}_{ij} \vec{\nabla}_j' U_{opt}'(\vec{r}_j', t) + \vec{\zeta}_i \tag{6.20}$$

Since we neglect the motion in the radial direction, we project Eq. (6.20) onto the azimuthal direction, whose axis is given by the unit vector $\hat{e}_{\varphi_i} = (-\sin\varphi_i, \cos\varphi_i)$. As illustrated in Fig. 6.1 (b), $\vec{\omega}$ is projected in the z direction ($\vec{\omega} = \omega \hat{e}_z$). Hence, Eq. (6.20) becomes:

$$R\frac{\mathrm{d}\varphi_i'}{\mathrm{d}t} = \omega R - \hat{e}_{\varphi_i'} \cdot \sum_{j=1}^{N} \vec{\mu}_{ij} \vec{\nabla}_j' U_{opt}'(\vec{r}_j', t) + \hat{e}_{\varphi_i'} \cdot \vec{\zeta}_i \tag{6.21}$$

The simulations performed to validate our analysis are based on Eq. (6.21). This equation describes the motion of particles in the reference frame corotating with the optical ring. In particular, it emphasizes the role of the potential barriers. In the extreme case we have no potential barriers, one would observe the maximum particle current in the corotating reference frame, corresponding to the rotation of the particles counterclockwise with angular velocity ωR. On the other hand, for sufficiently high barriers, particles would move along with the rotating traps, suppressing the particle current along the potential landscape.

6.3 Particle Size Effect on Transport

In this section, I present the experimental results of particle transport for diverse relative particle sizes. The used colloidal particles have a radius $a = 2\mu$m, and I keep constant the number of traps in the ring $N_{tr} = 27$. Here, I explore the cases of ring radius with values $R = 21.8\mu$m, 20.2μm, and 17.8μm, so the relative particle size to the potential landscape wavelength a/λ become 0.39, 0.43, and 0.48 respectively.

Again, to characterize the system, we focus on the current-density relations for various barrier heights U_0 in the corotating reference frame. We determine the particle density by the filling factor of the traps $\rho = N/N_{tr}$. We obtained the data of the currents from the particle trajectories (extracted from microscopy video-imaging) by determining the azimuthal velocities in the corotating frame for all particles. After averaging over time, we obtain the mean velocity of the particles $\langle v \rangle$ in the azimuthal direction and the current:

$$J(\rho) = \rho \frac{\langle v \rangle}{2\pi R} \tag{6.22}$$

Then, we normalized these currents with respect to the single particle current $J_0 = v_0/(2\pi R)$. The term v_0 is the single-particle velocity shown in Fig. 6.3.

We have seen in Section 5.2.1 that HI are decisive for suppressing the current at high particle densities. In contrast, in the absence of HI, the current increases with particle density at large ρ, which can be attributed to a cluster speed-up effect, as discussed in Refs. [104–106]. In Section 5.2.1, we also determined the influence of the HI on the barrier height enhancement in Eq. (5.5). Hence, such barrier enhancement should decelerate the motion, but it is not immediately evident why it leads to the jamming behavior.

We can understand such jamming-like behavior from the effective mean external potential $U_{eff}(\varphi')$ in the azimuthal direction in the corotating frame. In the absence of the driving, this potential is given by $U_{\varphi}^{st}(\varphi')$ of Eq. (6.8) with a HI-enhanced barrier height U_0^{HI} (we set the constant $c_0 = 0$ to match the experimental conditions). The flow-driving given by $(-\vec{\omega} \times \vec{r}') \simeq (-\omega_0 R\varphi')\hat{e}_{\varphi}$ in Eq. (6.19) corresponds to a constant torque $(-\omega_0 R^2/\mu_0)$. Accordingly, $U_{\varphi}^{st}(\varphi')$ becomes tilted in $(-\varphi')$-direction:

$$U_{eff}(\varphi') = \frac{U_0^{HI}}{2} \cos\left(N_{tr}\varphi'\right) + \frac{\omega R^2}{\mu_0}\varphi' \tag{6.23}$$

The external torque tilting restricts the appearance of potential minima in U_{eff} to cases where the potential barriers are sufficiently large, corresponding to the undercritical regime. In this regime, when a particle occupies a

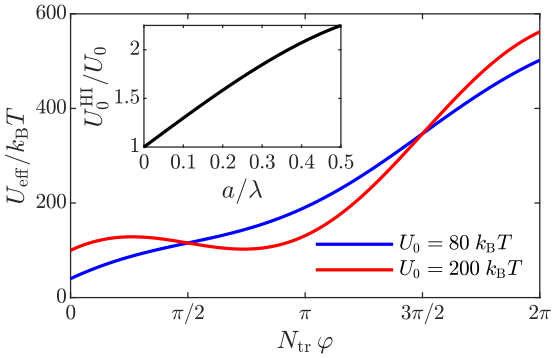

Figure 6.4: The effective potential of Eq. (6.23) in the corotating frame for two values of U_0. The data corresponds to the same number of optical traps $N_{tr} = 27$, ring radius $R = 20.2\mu$m, and angular frequency $\omega = 0.63$rad/s, yielding a tilting torque $\omega R^2/(N_{tr}\mu_0) \simeq 73.5 k_B T$. For this tilting torque, the effective potential starts exhibiting minima and maxima when $U_0 \gtrsim 147 k_B t$. Accordingly, for $U_0 = 80 k_B T$, the tilting is overcritical and U_{eff} varies monotonically with φ'. For $U_0 = 200 k_B T$ by contrast, the tilting is undercritical, and U_{eff} shows potential barriers. In the inset, I show the HI-induces barrier enhancement as predicted by Eq. (5.5) ($U_0^{HI}/U_0 \approx (1 + 3a/\lambda - 2a^3/\lambda^3)$.

potential well becomes an obstacle to the motion of neighboring particles (blocking effect), which leads to jamming at high particle densities.

Fig. 6.4 shows the effective potential of Eq. (6.23) for the overcritical ($U_0 = 80 k_B T$) and the undercritical ($U_0 = 200 k_B T$) regimes. The emergence of barriers occurs when U_0^{HI} is greater than a critical value U_{0c}^{HI}. In this situation, the particle motion shifts from a free motion along the potential landscape to surmounting barriers through thermally activated events occurring on large time scales. The critical barrier that promotes the change on the tilting regime $U_{0c}^{HI} = 2\omega R^2/(N_{tr}\mu_0) \simeq 147 k_B T$). Hence, due to the barrier height enhancement produced by the HI, the undercritical tilting

regime is reached at U_0 much smaller than U_{0c}.

According to the estimate in Eq. (5.5), the barrier enhancement should increase with the ratio a/λ for $a/\lambda \leq 1/2$, see the inset of Fig. 6.4, were I plot $U_0^{HI}/U_0 \approx (1 + 3a/\lambda - 2a^3/\lambda^3)$. Therefore, we expect the transition from over- to undercritical tilting shift toward smaller barrier heights U_0 with decreasing λ or decreasing ring radius R ($\lambda = 2\pi R/N_{tr}$).

In Fig 6.5, I show the experiments and simulations we carried out to check the previous hypothesis, showing the current-density curves for the radii $R = 17.8\mu$m, 20.2μm, and 21.8μm. To keep invariant the tilting in Eq. (6.23) and hence the drag torque on the particles, I adjust ω for each radius so that $\omega R^2 \simeq 257\mu\text{m}^2$ is constant. I show the experimental results in the upper row, while the simulated ones are in the lower row.

For all the studied radii, I observed jamming at sufficiently large ρ and barrier height U_0, whose values vary in each case. As expected, the experimental results show that jamming becomes more pronounced for smaller radii R or larger ratios a/λ.

In particular, for the biggest considered relative particle size $a/\lambda = 0.48$ ($R = 17.8\mu$m), one can observe jamming signatures even for the lowest barrier height $U_0 \simeq 80k_BT$. In this case, one can clearly appreciate jamming, finding similar results at intermediate barrier heights from 95 to $110k_BT$, where the current dramatically decreases after reaching the maximum value of $J(\rho)$. Such results resemble the ASEP model, so it may be indicative that the blocking effect is significant in this situation. For higher barrier heights, the maximum value of the current density migrates toward lower ρ regions, strongly reducing the particle current even when the particle occupancy is below half.

In contrast, in the smallest treated ratio $a/\lambda = 0.39$ ($R = 21.8\mu$m), the jamming bearly appears for barrier heights from 89 to $130k_BT$, and one can only clearly appreciate it for $U_0 = 140k_BT$, where the maximum current occurs at a low ρ value. One can also observe that $J(\rho)$ is close to the independent particle behavior for $U_0 \simeq 90k_BT$, diminishing progressively with increasing barrier height and acquiring a trend resembling the ASEP mechanism.

Between the extreme commented scenarios, we find the case of $a/\lambda = 0.43$

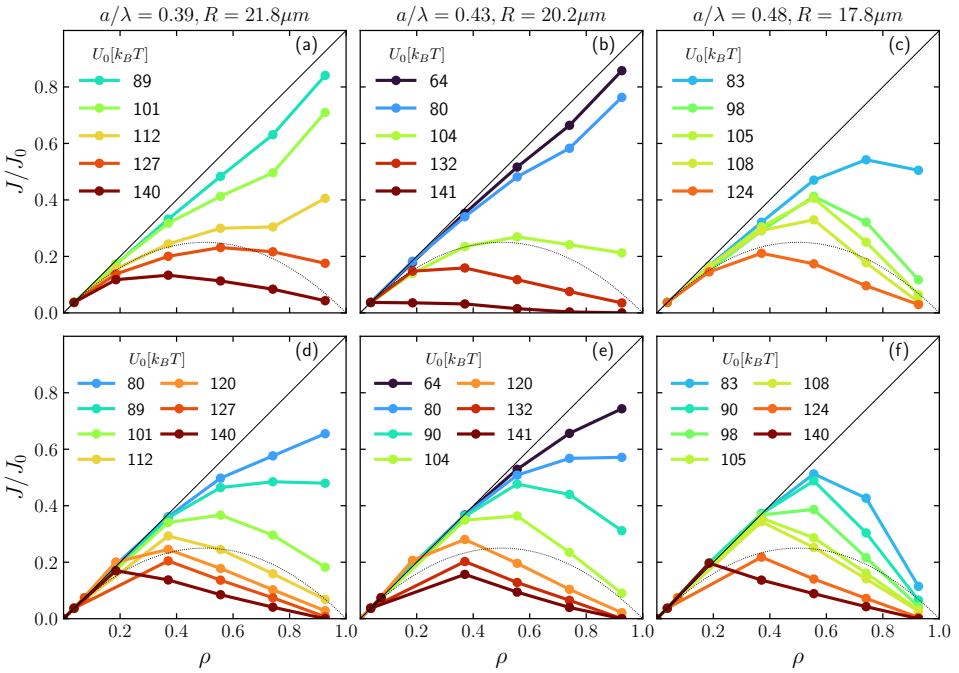

Figure 6.5: Experimental fundamental diagrams (upper row) in comparison with the simulated ones (lower row) for three different ring radii R (or particle radius a in units of the wavelength λ). Results correspond to a fixed number of optical traps $N_{tr} = 27$, various mean barrier heights U_0, and the same amplitude modulation $\xi = 0.22$ in all graphs. The angular frequency ω is such that $\omega R^2 \simeq 257\mu\text{m}^2/s$ is invariant, implying a constant tilting of the effective potential of Eq. (6.23), so the drag torque in the corotating reference frame is the same in all cases. The measured and simulated currents show qualitatively similar trends with jamming emerging at large ρ for sufficiently high mean barriers U_0. The value U_0 for the onset of the jamming behavior (transition from over- to undercritical tilting) shifts to smaller values for larger a/λ, as predicted from Eq. (5.5). In all the plots, the solid black lines mark the behavior for independent particles ($J(\rho)/J_0 = \rho$), and the thin dotted line indicates the current density function $\rho(1-\rho)$ predicted by the ASEP model.

($R = 20.2\mu$m). Here, $J(\rho)$ is close to the linear trend expected of independent particles for $U_0 \leq 80k_BT$. At higher barrier heights, the observed behavior is similar to that of $a/\lambda = 0.39$, but at a lower barrier height. Hence, the cases $U_0 = 132$ and $104k_BT$ for $a/\lambda = 0.43$ evoke the results found in $U_0 = 140$ and $127k_BT$ for $a/\lambda = 0.39$, respectively.

If we compare the experimental and simulated data for the same value U_0, we notice the presence of a quantitative mismatch. This issue can be due to the simplifications of the modeling, where we restricted the particle motion along the azimuthal direction and treated the HI approximately by the Blake tensor at the Rotne-Prager level.

One can notice that simulations tend to underestimate the particle current in all the analyzed situations, indicating a higher current suppression than the one observed in the experiments. The reason behind such underestimation could be ignoring experimental events that punctually increase the particle current. Examples may include cluster speed-up effects, like the collision between neighboring particles produced by the jump of a particle to an already occupied potential well. These events, arising from thermal fluctuations, occur with a very low probability but may be a source of the mismatching, especially at large ρ values, as the simulations implement severe constraints from the exclusion process.

6.4 Conclusions and Outlook

Transport overcoming potential barriers is widely present in nature. In this chapter, I have provided experimental results on how HI and particle size influence transport in the case of the Brownian motion of hard spheres driven across a periodic potential.

In our experiments, we implement a system of rotating optical traps that allow for studying particle transport under a vortex flow field. In the case of high potential barriers, I find that the currents strongly decrease with the particle density, reflecting jamming. This finding was interpreted by an effective HI-induced enhancement of the energetic barriers between the optical traps, which leads to a transition from an overcritical to an

undercritical tilting of the potential landscape. The interpretation of the jamming as a consequence of a HI-induced shift from over- to undercritical tilting of the optical potential provides an understanding of the experimental results.

Besides, I analyze the effect of the relative particle size by comparing the measured particle current for each situation. As expected, I reported that the HI-enhancement of the potential barriers is more pronounced with increasing the relative particle size. I also found signatures of a strong influence of the blocking mechanism when the particle radius a is close to $\lambda/2$, which slightly varied the multi-particle dynamics behavior compared to the two other exposed scenarios. The evidence presented for such affirmation derives from the similar behavior exhibited by $J(\rho)$ in a relatively wide range of potential barrier heights, namely from $U_0 \simeq 95$ to $110 K_B T$.

The presented experimental system can be extended in different directions. For example, the present work focuses on the flow-driven properties of monodispersed systems. One could ask how the collective dynamics and the reported jamming effect change in polydispersed systems with particles of different sizes. The simplest case would be to include one or a few differently-sized particles within the ring and to investigate how these inclusions behave by varying their relative fraction and the depth of the potential wells. Smaller or larger particles will see a different potential well than their neighbors, affecting their jumping over the potential barriers.

Further, modern colloid science allows the preparation of monodispersed particles with a shape that departs from the spherical one, such as ellipsoids [107] or cubes [108]. Using anisotropic colloids will increase the system's complexity when considering the generated HI but, on the other hand, will also allow us to experimentally extract the relative orientations of the particles within the ring. We could use this information to determine whether, in the steady state, such particles synchronize their rotational motion due to HI under the driving.

We could also change the nature of the particles, for example, using monodispersed paramagnetic colloids, which could be easily manipulated via magnetic fields in this geometry [109, 110]. One could increase the density of particles to induce jamming but using a rotating magnetic field [111, 112]

with opposite chirality to apply a torque which would un-jam the system.

Finally, instead of changing particles, the AOD can be programmed in such a way as to introduce a controlled degree of spatial or temporal disorder in the potential landscape, for example, by reducing or increasing the time that the laser beam visits one trap. One can also design a more complex optical path than the circular one, like elliptical or square, where the presence of sharp corners could induce earlier jamming or could act as a sink of particles that release them later at high angular speed.

Exploring these intriguing options will cultivate our understanding of HI effects in natural systems and could open ways toward their exploitation in technological applications.

Chapter 7

Fast Counterpropagating Solitons in Colloidal Systems

In previous chapters, I have discussed the importance of particle transport in condensed matter systems [113–115], since emerging phenomena from many-body effects appear in diverse systems. These systems vary from frictional atomic sliding [116, 117] to electron scattering [118–121], driven skyrmions [122, 123], and vortices in high-temperature superconductors [124–126]; liquid crystals [127], ultracold atoms [128], photonic [129–131], and active matter [132, 133].

In this context, in the previous chapters, I have focused on studying collective particle transport across periodic energy landscapes when these contain a number of particles lower than the potential wells. Here, I examine the situation of an overfilled potential landscape, where the periodic potential is loaded with particles over the number of available wells. Under this condition, I observed the appearance of counterpropagating solitons, which are stable cluster waves originating from a continuous particle exchange process.

In this chapter, I report the experimental dependence of the size and speed of the solitons with the particle diameter, which is supported by numerical simulations performed by the group of Prof. Philipp Maass at Osnabrük

University (Germany). I also examine the coexistence of several solitons and the interactions between them. These experiments demonstrate a generic mechanism for cluster-mediated transport with potential applications to other condensed matter systems on different length scales.

7.1 Introduction

When the transport of particles is due to an external force, different factors can influence their motion, including noise. However, in condensed matter systems, particle motion usually occurs across a potential landscape, like a crystalline surface, that may alter such transport. Examples include electrons moving in the potential created by an array of ions in a lattice [134] or motor proteins on a series of polar tracks [135, 136]. Prominent examples in soft matter systems include directional locking, which is the deviation of the particle motion from the force direction along a crystal axis [137–139], or pinning-depinning transition characterized by a complex alteration between static and dynamic modes [140–142].

Nevertheless, the movement of particles against the direction of the force is an unusual phenomenon reported only under specific conditions. These include the presence of intense confinement [143–145], multi-particle interactions [146], or under an external time-modulated potential [147, 148]. In most cases, however, the inversion of motion involved many particles rather than a small localized cluster.

Solitons are stable solitary waves propagating without distortion [149] that represent an alternative way matter can be transported at the microscale. They appear in diverse systems from fermionic superfluids [150] to Bose-Einstein condensates [151, 152], macroscopic cracks [153] and ocean waves [154]. In colloidal systems, stable solitons are difficult to be observed, especially when the particles are driven by periodic potentials. The difficulty follows from the fact that a soliton should contain a finite number of particles moving stably over an ensemble of passive ones. This situation is only possible when external forces due to optical tweezers [155] or external magnetic fields [156] are applied.

Here, I experimentally show how to create propagating solitons in a periodic potential created by a circular array of optical tweezers. The solitons emerge when I introduce more particles than potential wells, and they propagate against the driving direction, defined by the rotation of the optical ring. Further, the solitons reach higher speeds than that of the external driving. The observed solitons are dynamic clusters that continuously break and reform by releasing and accepting particles.

7.2 Soliton Observation

I show a scheme of the experimental setup in Fig. 7.1 (a), where one can see the collected particles inside a closed fluid cell trapped by the potential landscape. The fluid cell contains a water dispersion of polystyrene particles with diameter $\sigma = 4\mu$m. I create the potential landscape with the optical system presented in Chapter 4, which allows me to place $M = 27$ equispaced quasi-simultaneous optical traps along a circle of radius R. As a result, I obtain a quasi-one-dimensional periodic potential landscape with wavelength $\lambda = 2\pi R/M$ rotating at a constant angular velocity ω that confines N particles.

In this investigation, I explored different situations changing the relative particle diameter with respect to the potential wavelength, σ/λ. The experimental procedure consisted of varying the ring radius of the optical landscape without changing the number of optical traps M. Thus, λ changes and therefore does the coefficient σ/λ. However, as I changed the ring radius, I also needed to modify the angular velocity to obtain an equivalent torque for the different values of R. One can find the detailed parameters of the experiments in Tab. 7.1.

In this system, one can neglect the particle motion along the radial direction and focus only on the angular direction along the traveling-wave potential. The latter can be characterized mathematically as:

$$U(x,t) = \frac{U_0}{2}\cos\left[\frac{2\pi}{\lambda}(x+\omega R t)\right] \tag{7.1}$$

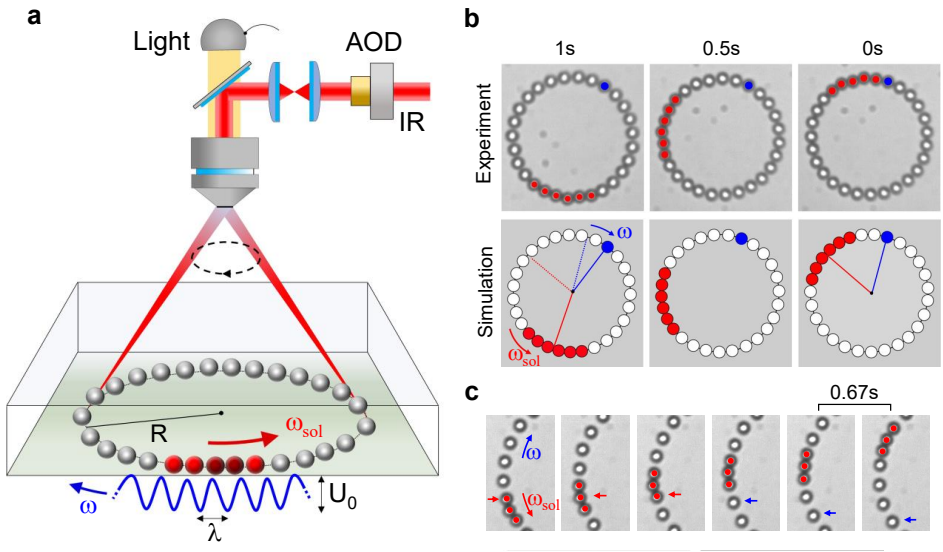

Figure 7.1: a) Scheme showing a ring of radius R with N colloidal particles of diameter σ trapped by a rotating periodic optical potential. I generate the potential landscape using an infrared laser (IR) passed through an Acousto Optic Deflector (AOD). The latter creates M equispaced traps at intervals $\lambda = 2\pi R/M$ and depth U_0, which slowly rotates clockwise with angular velocity ω. Particles highlighted in red belong to a counterclockwise propagating soliton. Two particles of the soliton marked in dark red occupy the same optical trap. b) Optical microscope (left) and simulation (right) images showing a particle cluster (red) counter-propagating with angular velocity ω_{sol} against the optical traps moving clockwise. The traps drag individual particles; one dragged particle is indicated in blue as a reference. The system parameters are $R = 20\mu$m, $M = 27$, $N = M + 1 = 28$, $\sigma = 0.86\lambda$, $\lambda = 4.7\mu$m, $\omega = 0.36$ rad/s, and $U_0 = 122 k_B T$. c) Sequence of images separated by 0.67 s for $\sigma = 0.6\lambda$, showing single particle attachments and detachments during soliton propagation.

Figures	M	$N-M$	σ/λ	$U_0/k_\mathrm{B}T$
7.1 (b), 7.1 (c)	27	1	0.86	122
7.1 (d)	19	1	0.60	211
7.2 (c), 7.2 (d), 7.3 (a)	21	1	0.67	179
7.2 (c), 7.2 (d)	24	1	0.76	158
7.3 (b)	22	1	0.6-0.85	176-124
7.4 (a), 7.4 (b)	21	1	0.67	179
	22	1	0.70	178
	23	1	0.73	165
	24	1	0.76	158
	25	1	0.80	140
	26	1	0.83	128
	27	1	0.86	122
7.5	21	1-4	0.67	179
	24	1-4	0.76	142
7.6	25	2	0.8	140
	21	3	0.67	179

Table 7.1: Parameters used to determine the different experimental conditions (also used in numerical simulations). M is the number of optical traps, $N-M$ is the overcrowding, and U_0/k_BT is the potential barrier between optical traps in units of thermal energy. The wavelength is $\lambda = 2\pi R/M$. Parameters that are kept constant in all experiments are $R = 20\,\mu$m, $\sigma = 4\,\mu$m, $\omega = 0.36\,$rad/s, and $D = 0.1295\,\mu\mathrm{m}^2/\mathrm{s}$.

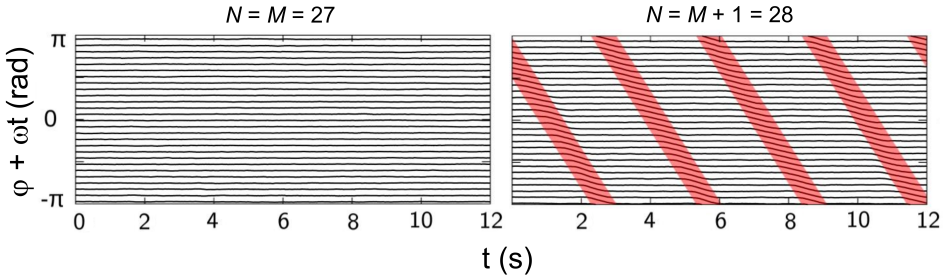

Figure 7.2: Temporal evolution of the angular particle coordinates $\varphi_i(t)$ in the reference frame corotating with the traps for the filled system ($N = M = 27$, left) and the overcrowded system ($N = M + 1 = 28$, right) of the images given in Fig. 7.1 (b). The emerging soliton is highlighted in red.

where $x = R\varphi$ with φ the azimuthal angle along the ring. This translating potential is responsible for the particle drag, and the angular velocity ω determines the regime of the particle transport. If ω is low, the particles can follow the movement of the potential wells, and they move at constant angular speed, so the particle current is maximum. When we increase ω, the viscous drag hinders the particle motion, decreasing the average velocity. Thus, the particle current decreases.

However, we have seen how HI induce jamming when the number of particles N approaches the number of potential wells M. In contrast, I find that when there are more particles than potential wells ($N > M$), the overcrowding promotes the generation of localized clusters that stably propagate along the ring without dispersion (Fig. 7.1 (b)). The cluster formation is not trivial since there are negligible attractive interactions between the colloidal particles.

Let me consider the case of one extra particle in the system, $N = M + 1$, which generates a double-occupied trap. In this situation, the surplus particle displaces the neighboring particles from their preferred position in the potential minima, which creates an extended defect, appearing as an almost compact cluster composed of particles that are almost in contact.

The defect propagates as a dispersion-free solitary wave (or soliton) along the optical ring. Surprisingly, the soliton propagation opposes the driving motion, achieving a much higher velocity than that imposed by the rotating potential.

7.3 Soliton Stability and Propagation

To understand the backward movement of the soliton propagation, one must consider a wavelike cooperative movement of the particles in the defect. During the process of defect propagation, there is a mechanism of detaching-attaching particles from the cluster. This way, the particles in the back end of the ensemble get detached, while the particles in the front end get attached as the potential landscape rotates (Fig. 7.1 (c)). Here, I refer to the back and front ends, taking as a reference the motion of the propagation of the defect. However, why do particles stay together without attractive interactions, and why does their cooperative movement appear as a stable soliton?

To answer these questions, I show in Fig. 7.2 the trajectories of the particles in a corotating reference frame with the optical traps. When the number of particles is equal to the number of potential wells, the particles perfectly follow the movement of the optical traps. On the other hand, when I add one extra particle to the system, one can see coherent particle movements between potential wells due to the soliton propagation, a situation highlighted by the red regions of the plot.

In the corotating reference frame, the fluid resistance, which opposes the motion with the potential rotation, tries to drive the particles in the clockwise direction, corresponding to the x-direction. The net force of the flow-driving follows from a coordinate transformation to the comoving frame: $x' = x + \omega R t$, yielding to $\mathrm{d}x'/\mathrm{d}t = \mathrm{d}x/\mathrm{d}t + \omega R$. Hence, this corresponds to a constant drag force $F = \omega R/\mu$ acting on the particles in the corotating reference frame, which tilts the periodic potential. For the parameters used in the experiments, the tilting is always in the undercritical regime, and the effective barrier between traps is much higher than the thermal energy $k_B T$.

Therefore, a single particle could only move between neighboring potential wells due to thermal activation. In the many-particle system with filling factor one ($N = M$), the drag force F does not promote any sustainable motion, as shown in Fig. 7.2.

In the case of an overcrowded system, the external fluid drag force contributes to the cluster stabilization, which we can express as $F^{ext}(x') = \omega R/\mu - \partial U(x')/\partial x'$, where $U(x') = (U_0/2)\cos(2\pi x'/\lambda)$ is the potential in the corotating reference frame. The condition on the external forces to hold n particles in an n-cluster is [105]:

$$\frac{1}{i}\sum_{j=1}^{i} F_j^{ext} \geq \frac{1}{n-i}\sum_{j=i+1}^{n} F_j^{ext}, \quad i = 1, \ldots, n-1 \tag{7.2}$$

Here, $F_j^{ext} = F^{ext}(x'_j)$ is the external force acting on the jth particle of the cluster. If the inequality 7.2 holds, cluster fragmentation is impossible. The fragmentation into a left subcluster of the first i particles and a right subcluster of the $(n-i)$ remaining particles would imply that the average force $\sum_{j=1}^{i} F_j^{ext}/i$ on the left subcluster would be smaller than the average force $\sum_{j=i+1}^{n} F_j^{ext}/(n-i)$ on the right subcluster.

Thus to maintain a stable cluster motion, Eq. 7.2 must be fulfilled for all points in some interval. If the interval spanned a period λ, the cluster would move without varying size. However, the soliton dynamics are complex, and the size of a cluster changes within λ, which leads to different types of solitons.

7.4 Types of solitons

As the potential barrier U_0 is much higher than $k_B T$, one can understand the formation and propagation of solitons by considering the limit of vanishing noise. Theoretical studies demonstrated that, in this limit, solitons consist of periodically repeating movements of clusters with different sizes [105, 106], whose equations of motions in the corotating frame are:

$$\frac{\mathrm{d}x_i'}{\mathrm{d}t} = \mu F^{ext}(x_i') = \omega R + \frac{\mu U_0 \pi}{\lambda} \sin\left(\frac{2\pi x_i'}{\lambda}\right) \tag{7.3}$$

Introducing scaled dimensionless coordinates and time, $x_i' \to y_i = x_i'/\lambda$, $t \to \lambda^2 t/(\pi\mu U_0)$, and a dimensionless driving force $f = \lambda\omega R/(\pi\mu U_0) = F\lambda/(\pi U_0)$, these equations become:

$$\frac{\mathrm{d}y_i}{\mathrm{d}t} = f + \sin(2\pi y_i) \tag{7.4}$$

Solving Eq. (7.4) under the conditions of one well with double occupancy and the external force actuation, after a transitory time, two soliton types with different motions appear as limit cycles: an A type soliton characterized by two subintervals of the movements of an n- and $(n+1)$-cluster during one period [n-($n+1$)-soliton] (Fig. 7.3 (a)), and a B type soliton formed by four subintervals of cluster movements [n-($n+1$)-($n+2$)-($n+1$)-soliton] (Fig. 7.3 (b)). We use the coordinate of the leftmost particle to define the position of a cluster.

The particle attachments and detachments to the cluster occur separately, so the cluster size changes discretely with one event at a time. The positions of a cluster are y_k, and t_k accounts for the time instants where an attachment or a detachment takes place, being k the label of each event. For example, in Fig. 7.3, $k = 1, 2$ for the type A soliton, and $k = 1, 2, 3, 4$ for the type B soliton.

Within one period of the motion of the type A soliton of size n, a single particle detaches at the back end of an $(n+1)$-cluster and attaches at the front end of an n-cluster. The back and front ends refer to the directions of the cluster motion in the corotating reference frame (this direction is positive, $x > 0$, for $f > 0$). In the case of the type B soliton, within one period of the motion, a single particle first detaches and attaches as in the case of type A, but in addition, the detached particle re-attaches at the back end of an $(n+1)$-cluster and, subsequently, detaches again. Type B solitons occur only in very determined conditions of particle sizes and driving forces, while the most common solitons are those of type A.

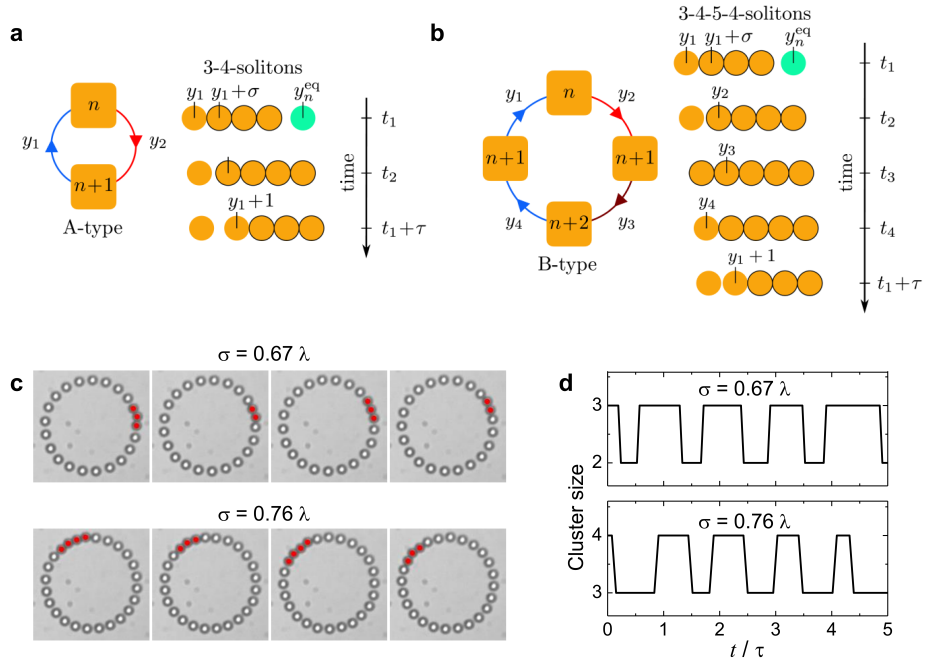

Figure 7.3: Soliton types and their observation. a) & b) Schemes showing two soliton types: a) type A soliton consisting of subsequent movements of an n- and $(n+1)$-cluster during one period, and b) type B soliton consisting of subsequent movements of four clusters. In both schemes, blue (red) arrows denote detachment (attachment) events of particles in the cluster. Framed circles represent those particles that keep in contact with progressing time. c) Experimental observation of a 3-2 soliton ($\sigma = 0.67\lambda$) and a 4-3 soliton ($\sigma = 0.76\lambda$). The particles that take part in the cluster formation are highlighted in red. d) Alternating cluster size for the two solitons as a function of the rescaled time t/τ, where $\tau = \lambda/v_{sol}$ is the soliton's time period. The detailed parameters for all the figures are those of Tab 7.1.

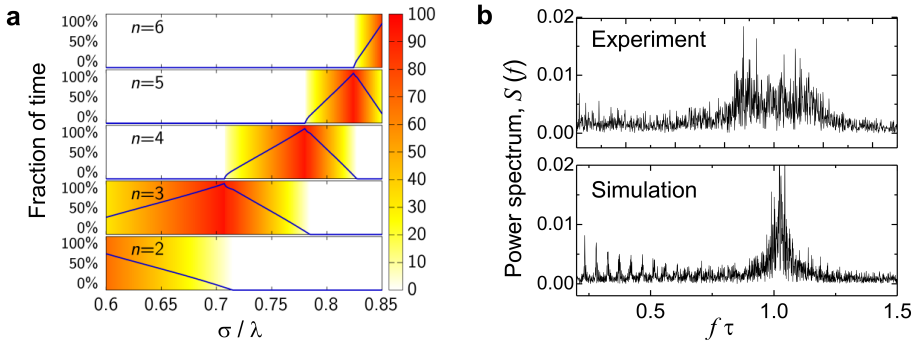

Figure 7.4: a) Fraction of time traversed by the n-clusters as a function of σ/λ calculated in the zero noise limit, represented by the blue lines and the color maps. b) Power spectra of soliton position versus scaled frequency $\nu\tau$ in experiments (top) and simulations (bottom). The detailed parameters for each situation are those of Tab 7.1.

Indeed, in the experiments, I observe the type A solitons: for $\sigma = 0.67\lambda$, sequences of 3- and 2-cluster movements occur, corresponding to a 3-2-soliton. Instead, for $\sigma = 0.76\lambda$, I observe the emergence of a 4-3-soliton (Fig. 7.3 (c)). In the analysis, the identification of a cluster proceeds from a sequence of neighboring particles whose separation is shorter than $5 \times 10^{-3}\lambda$. The number of n particles in the corresponding sequence determines the cluster size. To define the soliton position, we detect the pair of particles that share an optical trap as shown in Fig. 7.1 (a). The center of mass position of the two particles determines the soliton coordinate [angle coordinate $\varphi(t)$].

Fig. 7.3 (d) shows the time intervals of alternating n- and $(n+1)$-cluster motion. The duration of two consecutive time intervals is close to $\lambda/v_{sol} = \lambda/(\omega_{sol}R)$, which results from the underlying periodicity of the soliton motion. In the presence of noise, the movement is no longer perfectly periodic in time, but the power spectrum of the cluster position still reflects the underlying periodicity by exhibiting a peak at a frequency v_{sol}/λ. Indeed,

we find this peak in the spectrum in both experiments [Fig. 7.4 (b) top], and numerical simulations [Fig 7.4 (b) bottom]. In the spectra calculation, the relative position of the clusters to the next potential minimum was taken to filter out the trivial peak at frequency v_{sol}/L.

In Fig. 7.4 (a), I show the fraction of time a soliton stays in the n-cluster state as a function of the particle diameter. These results have been calculated analytically in the zero-noise limit. In particular, they demonstrate that the clusters of the solitons grow in size with increasing σ, in agreement with the experimental observations.

7.5 Soliton size and speed

In Fig. 7.5 (a), I show how the mean cluster size $\langle n \rangle$ increases with ω/λ. In the experiments (empty squares), I varied the wavelength λ according to $\lambda = 2\pi R/M$ with $M = [21, 27]$. The estimation of $\langle n \rangle$ derives from the assumption that an n-cluster extends a space $n\sigma$. Hence, the remaining $(N-n)$ particles not belonging to the n-cluster are close to potential minima and thus distributed over the length $(N-n)\lambda$. The two lengths should fill the ring of length $M\lambda = (N-1)\lambda$, which leads to $(N-n)\lambda + n\sigma \simeq (N-1)\lambda$, or the same $n\sigma \simeq (n-1)\lambda$. Generalizing this reasoning to any cluster in a soliton mode, one can find:

$$\langle n \rangle = \alpha \frac{1}{1 - \sigma/\lambda} \tag{7.5}$$

Where α is a prefactor of order unity. As shown in Fig. 7.5 (a), Eq. 7.5 with $\alpha = 0.83$ fits well the experimental data.

Fig. 7.5 (b) shows the normalized mean angular speed of the soliton ω_{sol}/ω as a function of the scaled particle diameter σ/λ, where the potential wavelength λ varies as in Fig. 7.5 (a). The observed speed raises nonlinearly with σ/λ, reaching a maximum value of $v_{sol} = 41.9\mu$m/s for $\lambda = 4.65\mu$m, which is almost six times higher than the optical landscape velocity in the opposite direction ($\omega R = 7.2\mu$m/s).

One could estimate the soliton mean velocity v_{sol} using a scaling argument

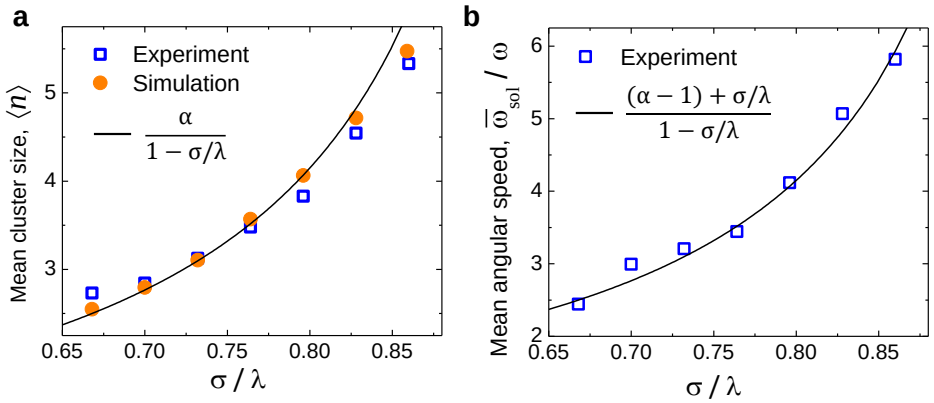

Figure 7.5: Soliton size and speed. a) Mean size $\langle n \rangle$ of clusters forming solitons as a function of σ/λ for M potential wells and $N = M + 1$ particles ($M = [21, 27]$). Empty squares are experimental data, filled circles are numerical simulations with the corresponding parameters similar to the experimental system, and the solid line corresponds to the theoretically predicted behavior of Eq. (7.5) with $\alpha = 0.83$. b) Normalized mean angular velocity $\bar{\omega}_{sol}/\omega$ of solitons as a function of σ/λ. Symbols mark experimental data, and the solid line is the theoretically predicted behavior according to Eq. (7.6). Further parameter details are in Tab. 7.1.

in the corotating reference frame. After the detachment and attachment of a particle, the mean distance a cluster moves is one wavelength λ. The required time for an attachment and detachment process is in the order of the mean distance $(\lambda - \sigma)$ between two particles divided by the velocity ωR. Accordingly, v_{sol} should be proportional to $\lambda\omega R/(\lambda - \sigma)$, so $v_{sol} \propto \omega R/(\lambda - \sigma) \propto \omega R\langle n\rangle$. An exact calculation of soliton velocities in the zero-noise limit supports this scaling argument, which in the laboratory frame is:

$$\omega_{sol} = \frac{v_{sol}}{R} - \omega = \frac{\alpha}{1 - \sigma/\lambda}\omega - \omega = \frac{(\alpha - 1) + \sigma/\lambda}{1 - \sigma/\lambda}\omega \tag{7.6}$$

Fig. 7.5 (b) shows that Eq. (7.6) accurately describes the mean soliton velocity found in the experiments.

7.6 Interaction between colloidal solitons

I find that in the experimental system is possible to generate more solitons simultaneously. In particular, the number of appearing solitons equals the overcrowding, defined as the difference $N - M$. Fig. 7.6 shows the increase of the number of solitons with $N - M$ for two cases of σ/λ. The observations suggest that solitons repel each other and propagate by keeping a well-defined mean distance. To quantify this effect, we analyzed the distributions of soliton distances.

I show in Fig. 7.7 the distribution $\psi(\Delta\varphi)$ of distances $\Delta\varphi(t) = |\varphi_2(t) - \varphi_1(t)|$ between the positions $\varphi_1(t)$ and $\varphi_2(t)$ of two solitons for experiments (top row), and simulations (bottom). In both cases, $\psi(\Delta\varphi)$ exhibits several peaks with a Gaussian-like envelope centered around a mean $\bar{\Delta\varphi} \simeq \pi$. This fine structure appears because of the preferential positions of the solitons around the potential minima, while other regions are less probable. Accordingly, the distance distribution shows peaks separated by $2\pi/M$. The localized envelope points out the existence of an effective repulsive soliton-soliton interaction, which tends to keep the positions of the solitons at a maximal distance π.

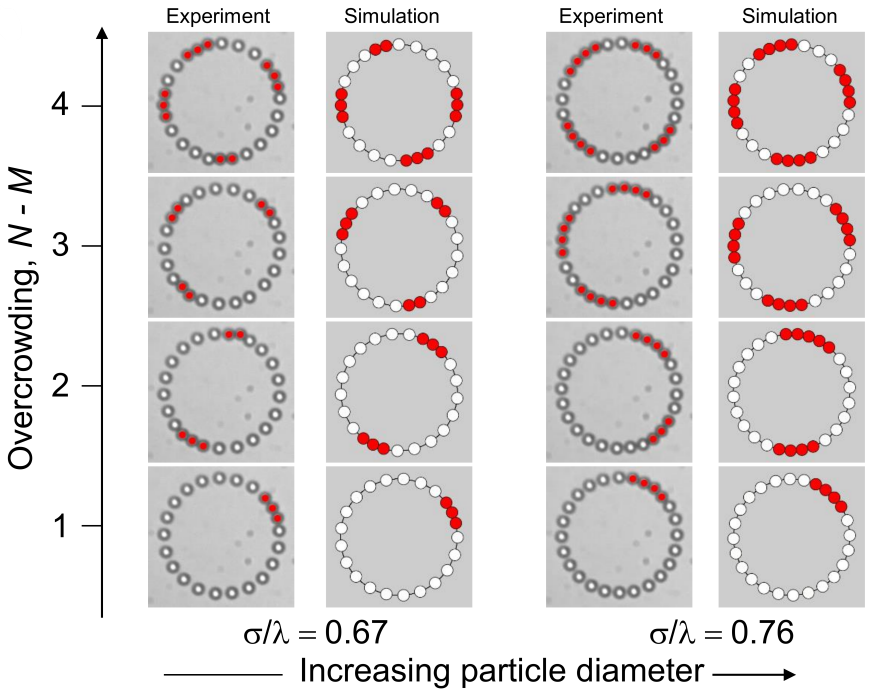

Figure 7.6: Number of solitons at different overcrowdings $N - M$ at two different scaled particle diameters σ/λ. The first (second) column shows experimental (simulation) images with solitons highlighted in red. Tab. 7.1 contains the detailed parameters of the experiments and simulations.

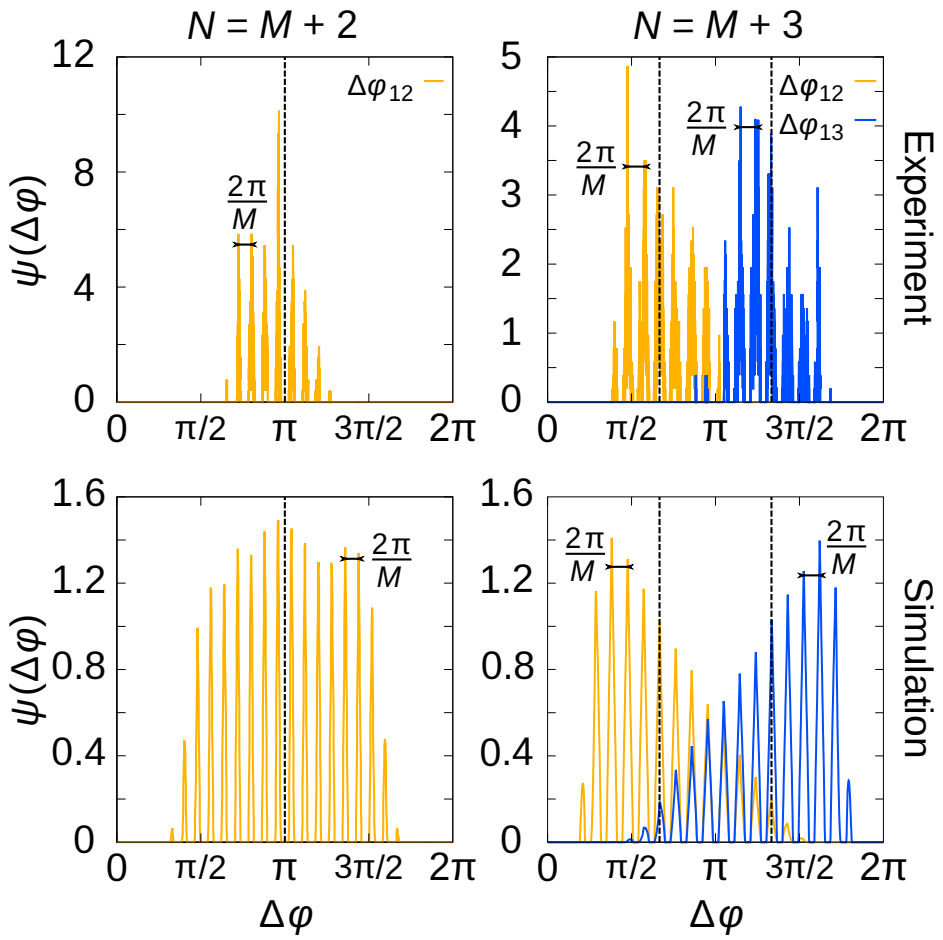

Figure 7.7: Distributions ψ of the phase differences $\Delta\varphi$ between two (left plots) and three (right plots) solitons for experiments (top) and numerical simulations (bottom). For two solitons, $\Delta\varphi = \Delta\varphi_{12}(t) = |\varphi_2(t) - \varphi_1(t)|$. For three solitons, $\Delta\varphi_{12}(t) = \varphi_2(t) - \varphi_1(t)$ and $\Delta\varphi_{13}(t) = \varphi_3(t) - \varphi_1(t)$, where the positions of the solitons are ordered according to $\varphi_1(t) < \varphi_2(t) < \varphi_3(t)$. In the left graphs, the dashed vertical lines mark the distance $\Delta\varphi = \pi$, while in the right graphs $\Delta\varphi = 2\pi/3$ and $\Delta\varphi = 4\pi/3$. Tab. 7.1 contains the detailed parameters of the experiments and simulations.

For steady states characterized by three propagating solitons, their positions can be ordered at each time t such that $\varphi_1(t) < \varphi_2(t) < \varphi_3(t)$. Accordingly, Fig. 7.7 the distributions $\Delta\varphi_{12}(t)$ and $\Delta\varphi_{13}(t)$ for the distances $\Delta\varphi_{12}(t) = \varphi_2(t) - \varphi_1(t)$ and $\Delta\varphi_{13}(t) = \varphi_3(t) - \varphi_1(t)$, respectively. In these cases, the envelopes of $\psi(\Delta\varphi_{12})$ and $\psi(\Delta\varphi_{13})$ are centered near the values $2\pi/3$ and $4\pi/3$.

7.7 Conclusions

In this chapter, I showed the experimental observation of solitary cluster waves in a highly crowded system of driven Brownian particles across a periodic potential. Strongly confined microscopic colloidal particles were forced to move along a ring of slowly rotating potential wells. In the overcrowded regime, where the number of particles exceeds the number of potential wells, solitary waves of particle clusters emerge. These solitons are robust and propagate against the rotation direction at speeds up to seven times higher than that of the potential landscape, offering an excellent method to transport matter under confinement.

The observed clusters form without the need for attractive interactions between particles but due to the external driving force. The cluster size varies during its motion, produced from an attachment-detachment process of the neighboring particles. As a result, the solitons consist of periodic sequences of particle clusters having different sizes. I also explained how to determine the main features of the clusters, including their size and velocity, using analytical calculations. Besides, the soliton features could be described by an analytical expression as a function of the particle size.

The experimental observations are supported by numerical simulations, which confirm the conclusions extracted from the experimental data. The simulations also allow us to explain the underlying physical mechanism of the system behavior with the analysis in the limit of small thermal fluctuations.

Moreover, I presented the observation of multiple solitons simultaneously in the system. This situation arises from system overcrowding, which generates one soliton for each extra particle exceeding the number of potential wells. When present, different solitons show an effective repulsive interaction between them.

Generally, solitons are waves without dispersion due to non-linear effects. Here, I experimentally demonstrate that it is possible to generate solitary cluster waves in a many-body system of overdamped Brownian particles, where inertia is negligible. I expect this transport mechanism is generic enough to be extended to other strongly confined dissipative systems under overcrowding conditions. Examples of such systems may include particles

flowing through porous media [157–159], high T_c vortices in heterostructures [160, 161], or self-propelling bacteria through small channels [162–164].

Particle transport in single-file conditions has attracted the attention of theoretical studies [79, 165–169], but it has found little attention from the experimental counterpart [60, 61, 170]. However, this work extends further the rich physics behind these confined systems. Specifically, this may be of keen interest when one intends to enhance transport through periodic potential barriers, a situation widely present nowadays in many artificial and biological systems, such as microfluidic channels or vein networks.

Chapter 8

Conclusions and Future Perspectives

In this thesis, I presented several experimental results focused on exploring the rich dynamics of driven and confined colloidal systems. All three Chapters 5, 6, and 7 have in common the transport of colloidal particles in periodic potentials. The optical tweezers have been the key to generating the periodic potential landscape, offering high versatility and control of the system conditions. With this technique, one can control the number of potential wells of the potential landscape, the barrier height between wells, the wavelength of the potential, and its rotation speed to induce the external driving force.

In Chapter 5, I presented the importance of the interactions mediated by the dispersing medium on particle transport. Inside a sinusoidal potential, the confined colloidal particles are restricted to moving along a line, so they cannot overpass each other. The effect of the external force through the fluid drag induces the movement of particles along the same direction, but the interaction of the particles with the fluid medium hinders the particle transport, causing jamming in the system.

When a fluid flow drives particles, the Hydrodynamic Interactions (HI) between neighboring particles induce a decrease in the drag force, which

makes it harder to overcome the potential barriers, decreasing the particle current. This result contrasts with the behavior of a force-driven system, in which the particle current increases with the effect of the HI. Both situations were presented and compared to explain the difference between flow- and force-driven mechanisms, highlighting the peculiarities of each type of transport and explaining the underlying physical mechanism observed in the experiments.

Motivated by these findings, in Chapter 6, I explored the system when the particle size varies. Specifically, the particle size changed compared to the potential wavelength, so keeping the number of potential wells while changing the optical ring radius allowed us to vary this feature within the rotating potential. This complementary study helped to understand that jamming increases when the relative particle size to the wavelength increases. The transport hampering is a consequence of the presence of HI between the particles, which induces an effective increase of the potential barrier. The potential wells are the stable positions of the colloidal particles. When the distance between wells is reduced (the relative particle size increases), particles get closer, blocking the particle transport.

However, we observed that transport hindering vanishes when the system becomes overcrowded. I investigated the overcrowding situation in Chapter 7, where I reported the emergence of solitary waves counterpropagating against the rotation of the potential landscape. The velocity of the solitons was observed to be up to seven times faster than the speed of the external potential driving. I then explain the characteristic features of the solitons, identifying their main properties (size and propagation speed) and connecting them to the relative particle size to the potential wavelength. Moreover, I reported the presence of effective repulsive interactions emerging when the system has multiple propagating solitons.

With these results, I have provided an exhaustive description of driven and confined colloidal systems in one-dimensional periodic potential landscapes. I obtained results that bring new phenomenology of particle transport in confined flow-driven systems, a research field with few experimental works.

Therefore, I expect the results of this thesis may be of interest to researchers working in diverse fields such as soft matter physics, biology,

microfluidics, and lab-on-a-chip devices. The system under study is general enough to easily extrapolate the obtained results to other condensed matter systems characterized by particle transport in a one-dimensional periodic potential.

However, there is still work to do beyond this system. Although I have achieved several results, some aspects need to improve. We witnessed that the potential landscape was not perfectly periodical, having a spatial modulation induced by the AOD deflection. Even though I proved that the spatial modulation did not interfere with the overall behavior, this is an undesired effect that one should avoid.

Moreover, it would be interesting to modify more features of the generated optical potential, for example, the potential well width given by the laser beam. This feature may introduce another control parameter on the optical potential landscape, making the system richer.

Also, there are other interesting situations that one could investigate without modifying the optical system. One could explore the transport dynamics of a bidisperse system of particles, the dynamics of particles with exotic shapes (squares, ellipses, peanuts...), or working with magnetic particles to induce long-range interactions. Despite the more complex physical mechanisms that such situations may introduce, the resulting emerging phenomena may justify their use.

Bibliography

[1] Sidney R. Nagel. "Experimental soft-matter science". In: *Reviews of Modern Physics* 89.2 (2017). ISSN: 15390756. DOI: 10.1103/RevModPhys.89.025002.

[2] Robert J. Hunter. *Introduction to modern colloid science*. eng. Repr. with. Oxford: Oxford University Press, 1994, p. 344. ISBN: 0198553862.

[3] Robert J. Hunter. *Foundations of colloid science*. eng. 2nd. Oxford: Oxford University Press, 2001, p. 806. ISBN: 0198505027.

[4] Milton Kerker. "Classics and classicists of colloid and interface science". In: *Journal of Colloid and Interface Science* 116.1 (1987), pp. 296–299. ISSN: 0021-9797. DOI: 10.1016/0021-9797(87)90123-8.

[5] Isaac Asimov. *Words of science, and the history behind them*. Riverside Press, 1959.

[6] Thomas Graham. "Liquid Diffusion Applied to Analysis". In: *Philosophical Transactions* 151 (1861), pp. 183–224.

[7] Robert Brown. "XXVII. A brief account of microscopical observations made in the months of June, July and August 1827, on the particles contained in the pollen of plants; and on the general existence of active molecules in organic and inorganic bodies". In: *The Philosophical Magazine* 4.21 (1828), pp. 161–173. DOI: 10.1080/14786442808674769.

[8] Jean Perrin. *Brownian Motion and Molecular Reality*. London: Taylor and Francis, 1910, p. 93.

[9] Louis G. Gouy. "Note sur le mouvement brownien". In: *Journal de Physique Théorique et Appliquée* 7.1 (1888), pp. 561–564. ISSN: 0368-3893. DOI: 10.1051/jphystap:018880070056101.

[10] W. B. Russel, D. A. Saville, and W. R. Schowalter. *Colloidal dispersions*. eng. Ed. by D. A. Saville and W. R. Schowalter. Cambridge monographs on mechanics and applied mathematics. Cambridge: Cambridge University Press, 1989, p. 525. ISBN: 0521426006.

[11] M. J. Lighthill. *Introduction to Fourier Analysis and Generalised Functions*. Cambridge University Press, 1958, pp. 10–14. ISBN: 9781139171427. DOI: https://doi.org/10.1017/CBO9781139171427.

[12] Kurt Jacobs. *Stochastic Processes for Physicists*. Cambridge University Press, 2010, p. 204. ISBN: 978-0-521-76542-8.

[13] Michel. Le Bellac, Fabrice Mortessagne, and G. George Batrouni. *Equilibrium and non-equilibrium statistical thermodynamics*. eng. Cambridge: Cambridge University Press, 2004, p. 616. ISBN: 0521821436.

[14] D. Babič, C. Schmitt, and C. Bechinger. "Colloids as model systems for problems in statistical physics". In: *Chaos* 15.2 (2005). ISSN: 10541500. DOI: 10.1063/1.1839311.

[15] Albert Einstein. "Über die von der molekularkinetischen Theorie der Wärme geforderte Bewegung von in ruhenden Flüssigkeiten suspendierten Teilchen". In: *Annalen der Physik* 322.8 (1905), pp. 549–560. ISSN: 1521-3889. DOI: 10.1002/ANDP.19053220806.

[16] Albert Einstein. "Eine neue Bestimmung der Moleküldimensionen". In: *Annalen der Physik* 19 (1906), pp. 289–306. ISSN: 10221360. DOI: 10.1002/masy.200550403.

[17] B. Derjaguin and L. Landau. "Theory of the stability of strongly charged lyophobic sols and of the adhesion of strongly charged particles in solutions of electrolytes". In: *Progress in Surface Science* 43.1-4 (1993), pp. 30–59. ISSN: 0079-6816. DOI: 10.1016/0079-6816(93)90013-L.

[18] B.W. Ninham. "On progress in forces since the DLVO theory". In: *Advances in Colloid and Interface Science* 83 (1999), pp. 1–17.

[19] E. J. W. Verwey and J. Th. G. Overbeek. *Theory of the Stability of Lyophobic Colloids*. Elsevier, 1948.

[20] Louis G. Gouy. "Sur la constitution de la charge électrique à la surface d'un électrolyte". In: *Journal de Physique Théorique et Appliquée* 9.1 (1910), pp. 457–468. ISSN: 0368-3893. DOI: 10.1051/JPHYSTAP:019100090045700.

[21] David Leonard Chapman. "A contribution to the theory of electrocapillarity". In: *Philosophical Magazine* 25.148 (2010), pp. 475–481. ISSN: 1941-5982. DOI: 10.1080/14786440408634187.

[22] Deborah Leckband and Jacob Israelachvili. "Intermolecular forces in biology". In: *Quarterly Reviews of Biophysics* 34.2 (2001), pp. 105–267. ISSN: 1469-8994. DOI: 10.1017/S0033583501003687.

[23] C. J. Lin, K. J. Lee, and N. F. Sather. "Slow motion of two spheres in a shear field". In: *Journal of Fluid Mechanics* 43.1 (1970), pp. 35–47. ISSN: 1469-7645. DOI: 10.1017/S0022112070002227.

[24] G. K. Batchelor and J. T. Green. "The hydrodynamic interaction of two small freely-moving spheres in a linear flow field". In: *Journal of Fluid Mechanics* 56.2 (1972), pp. 375–400. ISSN: 1469-7645. DOI: 10.1017/S0022112072002927.

[25] Sangtae Kim and Richard T. Mifflin. "The resistance and mobility functions of two equal spheres in low-Reynolds-number flow". In: *The Physics of Fluids* 28.7 (1998), p. 2033. ISSN: 0031-9171. DOI: 10.1063/1.865384.

[26] J. R. Blake. "A note on the image system for a stokeslet in a no-slip boundary". In: *Mathematical Proceedings of the Cambridge Philosophical Society* 70.2 (1971), pp. 303–310. ISSN: 1469-8064. DOI: 10.1017/S0305004100049902.

[27] Jens Rotne and Stephen Prager. "Variational Treatment of Hydrodynamic Interaction in Polymers". In: *The Journal of Chemical Physics* 50.11 (1969), p. 4831. ISSN: 0021-9606. DOI: 10.1063/1.1670977.

[28] Yann Von Hansen, Michael Hinczewski, and Roland R. Netz. "Hydrodynamic screening near planar boundaries: Effects on semiflexible polymer dynamics". In: *The Journal of Chemical Physics* 134.23 (2011), p. 235102. ISSN: 0021-9606. DOI: 10.1063/1.3593458.

[29] John Happel and Howard Brenner. *Low Reynolds Number Hydrodynamics*. Martinus Nijhoff Publishers, 1983.

[30] W. Hess and R. Klein. "Generalized hydrodynamics of systems of Brownian particles". In: *Advances in Physics* 32.2 (1983), pp. 173–283. ISSN: 14606976. DOI: 10.1080/00018738300101551.

[31] Jan K. G. Dhont. *An introduction to dynamics of colloids*. Elsevier, 1996, p. 642. ISBN: 9780444820099.

[32] A. Ashkin. "Acceleration and Trapping of Particles by Radiation Pressure". In: *Physical Review Letters* 24.4 (1970), pp. 156–159. ISSN: 00319007. DOI: 10.1103/PhysRevLett.24.156.

[33] Arthur Ashkin. "Atomic-Beam deflection by Resonance-Radiation Pressure". In: *Physical Review Letters* 25.19 (1970), pp. 1321–1324. ISSN: 2054-2070.

[34] Zev Bryant et al. "Structural transitions and elasticity from torque measurements on DNA". In: *Nature* 424.6946 (2003), pp. 338–341. ISSN: 1476-4687. DOI: 10.1038/nature01810.

[35] Steven B. Smith, Yujia Cui, and Carlos Bustamante. "Overstretching B-DNA: The Elastic Response of Individual Double-Stranded and Single-Stranded DNA Molecules". In: *Science* 271.5250 (1996), pp. 795–799. ISSN: 00368075. DOI: 10.1126/SCIENCE.271.5250.795.

[36] Yongli Zhang et al. "DNA translocation and loop formation mechanism of chromatin remodeling by SWI/SNF and RSC". In: *Molecular Cell* 24.4 (2006), pp. 559–568. ISSN: 10972765. DOI: 10.1016/j.molcel.2006.10.025.

[37] A. Mossa et al. "Dynamic force spectroscopy of DNA hairpins: I. Force kinetics and free energy landscapes". In: *Journal of Statistical Mechanics: Theory and Experiment* 2009.02 (2009), P02060. ISSN: 1742-5468. DOI: 10.1088/1742-5468/2009/02/P02060. arXiv: 0902.3632.

[38] M Manosas et al. "Dynamic force spectroscopy of DNA hairpins: II. Irreversibility and dissipation". In: *Journal of Statistical Mechanics: Theory and Experiment* 2009.02 (2009), P02061. ISSN: 1742-5468. DOI: 10.1088/1742-5468/2009/02/P02061.

[39] Miles Padgett and Roberto Di Leonardo. "Holographic optical tweezers and their relevance to lab on chip devices". In: *Lab on a Chip* 11.7 (2011), pp. 1196–1205. ISSN: 14730189. DOI: 10.1039/c0lc00526f.

[40] C. Lutz et al. "Diffusion of colloids in one-dimensional light channels". In: *Journal of Physics Condensed Matter* 16.38 (2004). ISSN: 09538984. DOI: 10.1088/0953-8984/16/38/022.

[41] Rongxin Huang et al. "Direct observation of the full transition from ballistic to diffusive Brownian motion in a liquid". In: *Nature Physics* 7 (2011), pp. 576–580. ISSN: 17452481. DOI: 10.1038/nphys1953.

[42] Chaolong Song, Nam Trung Nguyen, and Anand Krishna Asundi. "Optical alignment of a cylindrical object". In: *Journal of Optics A: Pure and Applied Optics* 11.3 (2009). ISSN: 14644258. DOI: 10.1088/1464-4258/11/3/034008.

[43] Miles Padgett and Richard Bowman. "Tweezers with a twist". In: *Nature Photonics* 5 (2011), pp. 343–348. ISSN: 17494885. DOI: 10.1038/nphoton.2011.81.

[44] M. P. MacDonald, G. C. Spalding, and K. Dholakia. "Microfluidic sorting in an optical lattice". In: *Nature* 426 (2003), pp. 421–424. ISSN: 00280836. DOI: 10.1038/nature02144.

[45] David G. Grier and Yael Roichman. "Holographic optical trapping". In: *Applied Optics* 45.5 (2006), pp. 880–887. ISSN: 15394522. DOI: 10.1364/AO.45.000880. arXiv: 0506284 [cond-mat].

[46] Yulia Sokolov et al. “Hydrodynamic pair attractions between driven colloidal particles”. In: *Physical Review Letters* 107.15 (2011), pp. 1–5. ISSN: 00319007. DOI: 10.1103/PhysRevLett.107.158302.

[47] C. Lutz et al. “Surmounting barriers: The benefit of hydrodynamic interactions”. In: *Europhysics Letters* 74.4 (2006), pp. 719–725. ISSN: 02955075. DOI: 10.1209/epl/i2006-10017-9.

[48] Mike Woerdemann et al. “Advanced optical trapping by complex beam shaping”. In: *Laser and Photonics Reviews* 7.6 (2013), pp. 839–854. ISSN: 18638880. DOI: 10.1002/lpor.201200058.

[49] Philip H. Jones, Onofrio M. Maragò, and Giovanni Volpe. *Optical Tweezers: Principles and Applications*. eng. Cambridge: Cambridge University Press, 2015. ISBN: 978-1-107-05116-4.

[50] Keir C. Neuman and Steven M. Block. “Optical trapping”. In: *Review of Scientific Instruments* 75.9 (2004), pp. 2787–2809. ISSN: 00346748. DOI: 10.1063/1.1785844.

[51] Bahaa E. A. Saleh. *Fundamentals of photonics*. eng. Ed. by Malvin Carl Teich. 2nd ed. Wiley series in pure and applied optics. Hoboken, New Jersey: John Wiley and Sons, 2007. ISBN: 9780471358329.

[52] Alexander Franzen. *ComponentLibrary: a free vector graphics library for optics*. 2006. URL: http://www.gwoptics.org/ComponentLibrary/ (visited on 01/05/2023).

[53] Anacnda Inc. *Anaconda Software Distribution*. 2020. URL: https://docs.anaconda.com/.

[54] Daniel B. Allan et al. *Trackpy*. 2021. DOI: https://doi.org/10.5281/zenodo.4682814.

[55] John C. Crocker and David G. Grier. “Methods of digital video microscopy for colloidal studies”. In: *Journal of Colloid and Interface Science* 179.1 (1996), pp. 298–310. ISSN: 00219797. DOI: 10.1006/jcis.1996.0217.

[56] Angeles I. Rodriguez-Villarreal et al. "An integrated detection method for flow viscosity measurements in microdevices". In: *IEEE Transactions on Biomedical Engineering* 68.7 (2021), pp. 2049–2057. ISSN: 15582531. DOI: 10.1109/TBME.2020.3013519.

[57] Julien Petit et al. "Vesicles-on-a-chip: A universal microfluidic platform for the assembly of liposomes and polymersomes". In: *The European Physical Journal E 2016 39:6* 39.6 (2016), pp. 1–6. ISSN: 1292-895X. DOI: 10.1140/EPJE/I2016-16059-8.

[58] Ming Ma et al. "Water transport inside carbon nanotubes mediated by phonon-induced oscillating friction". In: *Nature Nanotechnology* 10.8 (2015), pp. 692–695. ISSN: 1748-3395. DOI: 10.1038/NNANO.2015.134.

[59] Mahla Mirzaee-Kakhki et al. "Colloidal trains". In: *Soft Matter* 16.6 (2020), pp. 1594–1598. ISSN: 1744-6848. DOI: 10.1039/C9SM02261A. arXiv: 1911.06566.

[60] Christoph Lutz, Markus Kollmann, and Clemens Bechinger. "Single-file diffusion of colloids in one-dimensional channels". In: *Physical Review Letters* 93.2 (2004), p. 026001. ISSN: 00319007. DOI: 10.1103/PHYSREVLETT.93.026001/FIGURES/4/MEDIUM.

[61] Q. H. Wei, C. Bechinger, and P. Leiderer. "Single-file diffusion of colloids in one-dimensional channels". In: *Science* 287.5453 (2000), pp. 625–627. ISSN: 00368075. DOI: 10.1126/SCIENCE.287.5453.625/ASSET/D2B53CBE-47C6-41CA-A877-D4205F7EA421/ASSETS/GRAPHIC/SE0208219004.JPEG.

[62] M. H. van de (Marcel H.) Voorde and Bert Sels. *Nanotechnology in catalysis : applications in the chemical industry, energy development, and environment protection*. Wiley-VCH, Weinheim, 2017, p. 1190. ISBN: 978-3-527-33914-3.

[63] Songwei Zeng et al. "Selective Transport through the Ultrashort Carbon Nanotubes Embedded in Lipid Bilayers". In: *Journal of Physical Chemistry C* 122.48 (2018), pp. 27681–27688. ISSN: 19327455. DOI: 10.1021/ACS.JPCC.8B07861/ASSET/IMAGES/LARGE/JP-2018-078615_0002.JPEG.

[64] Michael Reichert and Holger Stark. "Circling particles and drafting in optical vortices". In: *Journal of Physics: Condensed Matter* 16.38 (2004), S4085. ISSN: 0953-8984. DOI: 10.1088/0953-8984/16/38/023. arXiv: 0405051 [cond-mat].

[65] Karolis Misiunas and Ulrich F. Keyser. "Density-Dependent Speed-up of Particle Transport in Channels". In: *Physical Review Letters* 122.21 (2019), p. 214501. ISSN: 10797114. DOI: 10.1103/PHYSREVLETT.122.214501/FIGURES/5/MEDIUM. arXiv: 1806.06448.

[66] K. Zahn, J. M. Méndez-Alcaraz, and G. Maret. "Hydrodynamic Interactions May Enhance the Self-Diffusion of Colloidal Particles". In: *Physical Review Letters* 79.1 (1997), p. 175. ISSN: 10797114. DOI: 10.1103/PhysRevLett.79.175.

[67] B. Rinn et al. "Influence of hydrodynamic interactions on the dynamics of long-range interacting colloidal particles". In: *Europhysics Letters* 46.4 (1999), p. 537. ISSN: 0295-5075. DOI: 10.1209/EPL/I1999-00297-5.

[68] Paolo Malgaretti, Ignacio Pagonabarraga, and Daan Frenkel. "Running Faster Together: Huge Speed up of Thermal Ratchets due to Hydrodynamic Coupling". In: *Physical Review Letters* 109.16 (2012), p. 168101. ISSN: 00319007. DOI: 10.1103/PHYSREVLETT.109.168101/FIGURES/5/MEDIUM. arXiv: 1209.4189.

[69] Harel Nagar and Yael Roichman. "Collective excitations of hydrodynamically coupled driven colloidal particles". In: *Physical Review E* 90.4 (2014), p. 042302. ISSN: 15502376. DOI: 10.1103/PHYSREVE.90.042302/FIGURES/7/MEDIUM. arXiv: 1312.6576.

[70] Andrej Grimm and Holger Stark. "Hydrodynamic interactions enhance the performance of Brownian ratchets". In: *Soft Matter* 7.7 (2011), pp. 3219–3227. ISSN: 1744-6848. DOI: 10.1039/C0SM01085E.

[71] Marcel Dierl, Philipp Maass, and Mario Einax. "Classical driven transport in open systems with particle interactions and general couplings to reservoirs". In: *Physical Review Letters* 108.6 (2012),

p. 060603. ISSN: 00319007. DOI: 10.1103/PHYSREVLETT.108.060603/FIGURES/3/MEDIUM.

[72] Michael P. N. Juniper et al. "Acousto-optically generated potential energy landscapes: Potential mapping using colloids under flow". In: *Optics Express* 20.27 (2012), pp. 28707–28716. ISSN: 1094-4087. DOI: 10.1364/OE.20.028707.

[73] Andreas Schadschneider, Debashish Chowdhury, and Katsuhiro Nishinari. *Stochastic transport in complex systems: From molecules to vehicles*. 3rd. Amsterdam: Elsevier, 2010, pp. 1–557. ISBN: 9780444528537.

[74] B. Derrida. "An exactly soluble non-equilibrium system: The asymmetric simple exclusion process". In: *Physics Reports* 301.1-3 (1998), pp. 65–83. ISSN: 0370-1573. DOI: 10.1016/S0370-1573(98)00006-4.

[75] G. M. Schütz. "Exactly Solvable Models for Many-Body Systems Far from Equilibrium". In: *Phase Transitions and Critical Phenomena* 19.C (2001), pp. 1–251. ISSN: 1062-7901. DOI: 10.1016/S1062-7901(01)80015-X.

[76] Donald L. Ermak and J. A. McCammon. "Brownian dynamics with hydrodynamic interactions". In: *The Journal of Chemical Physics* 69.4 (2008), p. 1352. ISSN: 0021-9606. DOI: 10.1063/1.436761.

[77] Sangtae. Kim and Seppo J. Karrila. *Microhydrodynamics : principles and selected applications*. Butterworth-Heinemann, 1991, p. 507. ISBN: 9780750691734.

[78] Dominik Lips, Artem Ryabov, and Philipp Maass. "Brownian Asymmetric Simple Exclusion Process". In: *Physical Review Letters* 121.16 (2018), p. 160601. ISSN: 10797114. DOI: 10.1103/PHYSREVLETT.121.160601/FIGURES/4/MEDIUM. arXiv: 1807.00138.

[79] Dominik Lips, Artem Ryabov, and Philipp Maass. "Single-file transport in periodic potentials: The Brownian asymmetric simple exclusion process". In: *Physical Review E* 100.5 (2019), p. 052121. ISSN: 24700053. DOI: 10.1103/PHYSREVE.100.052121/FIGURES/11/MEDIUM. arXiv: 1906.08493.

[80] Eric Lauga and Thomas R. Powers. "The hydrodynamics of swimming microorganisms". In: *Reports on Progress in Physics* 72.9 (2009), p. 096601. ISSN: 0034-4885. DOI: 10.1088/0034-4885/72/9/096601. arXiv: 0812.2887.

[81] Ingmar H. Riedel, Karsten Kruse, and Jonathon Howard. "A self-organized vortex array of hydrodynamically entrained sperm cells". In: *Science (New York, N.Y.)* 309.5732 (2005), pp. 300–303. ISSN: 1095-9203. DOI: 10.1126/SCIENCE.1110329.

[82] C. J. Pierce et al. "Hydrodynamic Interactions, Hidden Order, and Emergent Collective Behavior in an Active Bacterial Suspension". In: *Physical Review Letters* 121.18 (2018), p. 188001. ISSN: 10797114. DOI: 10.1103/PHYSREVLETT.121.188001/FIGURES/4/MEDIUM.

[83] Eric Lauga et al. "Swimming in circles: motion of bacteria near solid boundaries". In: *Biophysical journal* 90.2 (2006), pp. 400–412. ISSN: 0006-3495. DOI: 10.1529/BIOPHYSJ.105.069401.

[84] Allison P. Berke et al. "Hydrodynamic attraction of swimming microorganisms by surfaces". In: *Physical Review Letters* 101.3 (2008), p. 038102. ISSN: 00319007. DOI: 10.1103/PHYSREVLETT.101.038102/FIGURES/3/MEDIUM. arXiv: 0806.2898.

[85] R. Di Leonardo et al. "Swimming with an image". In: *Physical Review Letters* 106.3 (2011), p. 038101. ISSN: 00319007. DOI: 10.1103/PHYSREVLETT.106.038101/FIGURES/3/MEDIUM.

[86] M. Reichert and H. Stark. "Synchronization of rotating helices by hydrodynamic interactions". In: *The European Physical Journal E* 17.4 (2005), pp. 493–500. ISSN: 1292-895X. DOI: 10.1140/EPJE/I2004-10152-7.

[87] Andrej Vilfan and Frank Jülicher. "Hydrodynamic flow patterns and synchronization of beating cilia". In: *Physical Review Letters* 96.5 (2006), p. 058102. ISSN: 10797114. DOI: 10.1103/PHYSREVLETT.96.058102/FIGURES/4/MEDIUM.

[88] Knut Drescher et al. "Dancing volvox: Hydrodynamic bound states of swimming algae". In: *Physical Review Letters* 102.16 (2009), p. 168101. ISSN: 00319007. DOI: 10.1103/PHYSREVLETT.102.168101/FIGURES/5/MEDIUM. arXiv: 0901.2087.

[89] Nariya Uchida and Ramin Golestanian. "Generic conditions for hydrodynamic synchronization". In: *Physical Review Letters* 106.5 (2011), p. 058104. ISSN: 00319007. DOI: 10.1103/PHYSREVLETT.106.058104/FIGURES/3/MEDIUM. arXiv: 1011.1134.

[90] Yulia Sokolov et al. "Hydrodynamic pair attractions between driven colloidal particles". In: *Physical Review Letters* 107.15 (2011), p. 158302. ISSN: 00319007. DOI: 10.1103/PHYSREVLETT.107.158302/FIGURES/4/MEDIUM.

[91] Douglas R. Brumley et al. "Hydrodynamic synchronization and metachronal waves on the surface of the colonial alga Volvox carteri". In: *Physical Review Letters* 109.26 (2012), p. 268102. ISSN: 00319007. DOI: 10.1103/PHYSREVLETT.109.268102/FIGURES/4/MEDIUM.

[92] Brato Chakrabarti and David Saintillan. "Hydrodynamic Synchronization of Spontaneously Beating Filaments". In: *Physical Review Letters* 123.20 (2019), p. 208101. ISSN: 10797114. DOI: 10.1103/PHYSREVLETT.123.208101/FIGURES/4/MEDIUM. arXiv: 1904.10088.

[93] P. N. Segrè, E. Herbolzheimer, and P. M. Chaikin. "Long-Range Correlations in Sedimentation". In: *Physical Review Letters* 79.13 (1997), p. 2574. ISSN: 10797114. DOI: 10.1103/PhysRevLett.79.2574.

[94] P. N. Segrè et al. "An effective gravitational temperature for sedimentation". In: *Nature* 409.6820 (2001), pp. 594–597. ISSN: 0028-0836. DOI: 10.1038/35054518.

[95] J. T. Padding and A. A. Louis. "Hydrodynamic and Brownian fluctuations in sedimenting suspensions". In: *Physical Review Letters* 93.22 (2004), p. 220601. ISSN: 00319007. DOI: 10.1103/PHYSREVLETT.93.220601/FIGURES/4/MEDIUM. arXiv: 0409133 [cond-mat].

[96] Bianxiao Cui, Haim Diamant, and Binhua Lin. "Screened Hydrodynamic Interaction in a Narrow Channel". In: *Physical Review Letters* 89.18 (2002), p. 188302. ISSN: 10797114. DOI: 10.1103/PHYSREVLETT.89.188302/FIGURES/4/MEDIUM. arXiv: 0205386 [cond-mat].

[97] Bianxiao Cui et al. "Anomalous hydrodynamic interaction in a Quasi-two-dimensional suspension". In: *Physical Review Letters* 92.25 I (2004), p. 258301. ISSN: 00319007. DOI: 10.1103/PHYSREVLETT.92.258301/FIGURES/4/MEDIUM. arXiv: 0312298 [cond-mat].

[98] Xinliang Xu et al. "Influence of hydrodynamic coupling on pair diffusion in a quasi-one-dimensional colloid system". In: *Physical Review Letters* 95.15 (2005), p. 158301. ISSN: 00319007. DOI: 10.1103/PHYSREVLETT.95.158301/FIGURES/3/MEDIUM.

[99] Bartosz A. Grzybowski, Howard A. Stone, and George M. Whitesides. "Dynamic self-assembly of magnetized, millimetre-sized objects rotating at a liquid–air interface". In: *Nature* 405 (2000), pp. 1033–1036. ISSN: 1476-4687. DOI: 10.1038/35016528.

[100] Peter Lenz et al. "Membranes with Rotating Motors". In: *Physical Review Letters* 91.10 (2003), p. 108104. ISSN: 10797114. DOI: 10.1103/PhysRevLett.91.108104.

[101] M. Radu and T. Schilling. "Solvent hydrodynamics speed up crystal nucleation in suspensions of hard spheres". In: *Europhysics Letters* 105.2 (2014), p. 26001. ISSN: 0295-5075. DOI: 10.1209/0295-5075/105/26001. arXiv: 1301.5592.

[102] Michio Tateno et al. "Influence of Hydrodynamic Interactions on Colloidal Crystallization". In: *Physical Review Letters* 123.25 (2019), p. 258002. ISSN: 10797114. DOI: 10.1103/PHYSREVLETT.123.258002/FIGURES/3/MEDIUM.

[103] Michael P.N. Juniper et al. "Colloidal particles driven across periodic optical-potential-energy landscapes". In: *Physical Review E* 93.1 (2016), p. 012608. ISSN: 24700053. DOI: 10.1103/PHYSREVE.93.012608/FIGURES/7/MEDIUM.

[104] Dominik Lips et al. "Emergent colloidal currents across ordered and disordered landscapes". In: *Communications Physics* 4.1 (2021), pp. 1–8. ISSN: 2399-3650. DOI: 10.1038/s42005-021-00722-0.

[105] Alexander P. Antonov, Artem Ryabov, and Philipp Maass. "Solitons in Overdamped Brownian Dynamics". In: *Physical Review Letters* 129.8 (2022), p. 080601. ISSN: 10797114. DOI: 10.1103/PHYSREVLETT.129.080601/FIGURES/4/MEDIUM. arXiv: 2204.14181.

[106] Alexander P. Antonov et al. "Collective excitations in jammed states: ultrafast defect propagation and finite-size scaling". In: *New Journal of Physics* 24.9 (2022), p. 093020. ISSN: 1367-2630. DOI: 10.1088/1367-2630/AC8E26. arXiv: 2203.06372.

[107] Julie A. Champion, Yogesh K. Katare, and Samir Mitragotri. "Making polymeric micro- and nanoparticles of complex shapes". In: *Proceedings of the National Academy of Sciences of the United States of America* 104.29 (2007), pp. 11901–11904. ISSN: 0027-8424. DOI: 10.1073/PNAS.0705326104.

[108] Laura Rossi et al. "Cubic crystals from cubic colloids". In: *Soft Matter* 7.9 (2011), pp. 4139–4142. ISSN: 1744-6848. DOI: 10.1039/C0SM01246G.

[109] Antonio Ortiz-Ambriz et al. "Laning, thinning and thickening of sheared colloids in a two-dimensional Taylor–Couette geometry". In: *Soft Matter* 14.24 (2018), pp. 5121–5129. ISSN: 1744-6848. DOI: 10.1039/C8SM00434J. arXiv: 1710.11156.

[110] Sascha Gerloff et al. "Dynamical modes of sheared confined microscale matter". In: *Soft Matter* 16.41 (2020), pp. 9423–9435. ISSN: 1744-6848. DOI: 10.1039/D0SM01238F. arXiv: 2007.04601.

[111] Pietro Tierno, Ramanathan Muruganathan, and Thomas M. Fischer. "Viscoelasticity of dynamically self-assembled paramagnetic colloidal clusters". In: *Physical Review Letters* 98.2 (2007), p. 028301. ISSN: 00319007. DOI: 10.1103/PHYSREVLETT.98.028301/FIGURES/4/MEDIUM.

[112] Fernando Martinez-Pedrero et al. "Colloidal Microworms Propelling via a Cooperative Hydrodynamic Conveyor Belt". In: *Physical Review Letters* 115.13 (2015), p. 138301. ISSN: 10797114. DOI: 10.1103/PHYSREVLETT.115.138301/FIGURES/4/MEDIUM.

[113] Peter Reimann. "Brownian motors: noisy transport far from equilibrium". In: *Physics Reports* 361.2-4 (2002), pp. 57–265. ISSN: 0370-1573. DOI: 10.1016/S0370-1573(01)00081-3. arXiv: 0010237 [cond-mat].

[114] Peter Hänggi and Fabio Marchesoni. "Artificial Brownian motors: Controlling transport on the nanoscale". In: *Reviews of Modern Physics* 81.1 (2009), pp. 387–442. ISSN: 00346861. DOI: 10.1103/REVMODPHYS.81.387/FIGURES/39/MEDIUM. arXiv: 0807.1283.

[115] C. Reichhardt and C. J. Olson Reichhardt. "Depinning and nonequilibrium dynamic phases of particle assemblies driven over random and ordered substrates: a review". In: *Reports on Progress in Physics* 80.2 (2016), p. 026501. ISSN: 0034-4885. DOI: 10.1088/1361-6633/80/2/026501. arXiv: 1602.03798.

[116] Andrea Vanossi et al. "Colloquium: Modeling friction: From nanoscale to mesoscale". In: *Reviews of Modern Physics* 85.2 (2013), pp. 529–552. ISSN: 00346861. DOI: 10.1103/REVMODPHYS.85.529/FIGURES/14/MEDIUM.

[117] Oded Hod et al. "Structural superlubricity and ultralow friction across the length scales". In: *Nature* 563.7732 (2018), pp. 485–492. ISSN: 1476-4687. DOI: 10.1038/s41586-018-0704-z.

[118] J. Voit et al. "Electronic structure of solids with competing periodic potentials". In: *Science* 290.5491 (2000), pp. 501–503. ISSN: 00368075. DOI: 10.1126/SCIENCE.290.5491.501/ASSET/AC6D806C-EFE9-41D7-84FB-F34ED435B3EF/ASSETS/GRAPHIC/SE4008907004.JPEG.

[119] Bin Li et al. "Ultrafast interfacial proton-coupled electron transfer". In: *Science* 311.5766 (2006), pp. 1436–1440. ISSN: 00368075. DOI: 10.1126/SCIENCE.1122190/ASSET/E90EE293-FA54-4B2C-B5C8-C2EE48332599/ASSETS/GRAPHIC/311_1436_F4.JPEG.

[120] W. Kuehn et al. "Coherent ballistic motion of electrons in a periodic potential". In: *Physical Review Letters* 104.14 (2010), p. 146602. ISSN: 00319007. DOI: 10.1103/PHYSREVLETT.104.146602/FIGURES/3/MEDIUM.

[121] James P. Custer et al. "Ratcheting quasi-ballistic electrons in silicon geometric diodes at room temperature". In: *Science* 368.6487 (2020), pp. 177–180. ISSN: 10959203. DOI: 10.1126/SCIENCE.AAY8663/SUPPL_FILE/AAY8663_CUSTER_SM.PDF.

[122] S. Mühlbauer et al. "Skyrmion lattice in a chiral magnet". In: *Science* 323.5916 (2009), pp. 915–919. ISSN: 00368075. DOI: 10.1126/SCIENCE.1166767/SUPPL_FILE/MUEHLBAUER.SOM.PDF. arXiv: 0902.1968.

[123] C. Reichhardt, C. J.O. Reichhardt, and M. V. Milošević. "Statics and dynamics of skyrmions interacting with disorder and nanostructures". In: *Reviews of Modern Physics* 94.3 (2022), p. 035005. ISSN: 15390756. DOI: 10.1103/REVMODPHYS.94.035005/FIGURES/74/MEDIUM.

[124] G. Blatter et al. "Vortices in high-temperature superconductors". In: *Reviews of Modern Physics* 66.4 (1994), p. 1125. ISSN: 00346861. DOI: 10.1103/RevModPhys.66.1125.

[125] K. Harada et al. "Direct Observation of Vortex Dynamics in Superconducting Films with Regular Arrays of Defects". In: *Science* 274.5290 (1996), pp. 1167–1170. ISSN: 00368075. DOI: 10.1126/SCIENCE.274.5290.1167.

[126] J. E. Villegas et al. "A Superconducting Reversible Rectifier That Controls the Motion of Magnetic Flux Quanta". In: *Science* 302.5648 (2003), pp. 1188–1191. ISSN: 00368075. DOI: 10.1126/SCIENCE.1090390/SUPPL_FILE/VILLEGAS.SOM.PDF.

[127] A. Duzgun et al. "Commensurate states and pattern switching via liquid crystal skyrmions trapped in a square lattice". In: *Soft Matter* 16.13 (2020), pp. 3338–3343. ISSN: 1744-6848. DOI: 10.1039/C9SM02312G. arXiv: 1911.10270.

[128] Immanuel Bloch. "Quantum coherence and entanglement with ultracold atoms in optical lattices". In: *Nature* 453.7198 (2008), pp. 1016–1022. ISSN: 1476-4687. DOI: 10.1038/nature07126.

[129] Peng Wang et al. "Localization and delocalization of light in photonic moiré lattices". In: *Nature* 577.7788 (2019), pp. 42–46. ISSN: 1476-4687. DOI: 10.1038/s41586-019-1851-6. arXiv: 2009.08131.

[130] Demetrios N. Christodoulides, Falk Lederer, and Yaron Silberberg. "Discretizing light behaviour in linear and nonlinear waveguide lattices". In: *Nature* 424.6950 (2003), pp. 817–823. ISSN: 1476-4687. DOI: 10.1038/nature01936.

[131] Marius Jürgensen, Sebabrata Mukherjee, and Mikael C. Rechtsman. "Quantized nonlinear Thouless pumping". In: *Nature* 596.7870 (2021), pp. 63–67. ISSN: 1476-4687. DOI: 10.1038/s41586-021-03688-9. arXiv: 2106.14128.

[132] Clemens Bechinger et al. "Active particles in complex and crowded environments". In: *Reviews of Modern Physics* 88.4 (2016), p. 045006. ISSN: 15390756. DOI: 10.1103/REVMODPHYS.88.045006/FIGURES/33/MEDIUM. arXiv: 1602.00081.

[133] C. J.Olson Reichhardt and C. Reichhardt. "Ratchet Effects in Active Matter Systems". In: *Annual Review of Condensed Matter Physics* 8 (2017), pp. 51–75. ISSN: 19475462. DOI: 10.1146/ANNUREV-CONMATPHYS-031016-025522. arXiv: 1604.01072.

[134] J. C. Slater. "Wave Functions in a Periodic Potential". In: *Physical Review* 51.10 (1937), p. 846. ISSN: 0031899X. DOI: 10.1103/PhysRev.51.846.

[135] T. Kreis and R. Vale. *Cytoskeletal and Motor Proteins*. 2nd. New York: Oxford University Press, 1993.

[136] Frank Jülicher, Armand Ajdari, and Jacques Prost. "Modeling molecular motors". In: *Reviews of Modern Physics* 69.4 (1997), p. 1269. ISSN: 00346861. DOI: 10.1103/RevModPhys.69.1269.

[137] C. Reichhardt and Franco Nori. "Phase Locking, Devil's Staircases, Farey Trees, and Arnold Tongues in Driven Vortex Lattices with Periodic Pinning". In: *Physical Review Letters* 82.2 (1999), p. 414. ISSN: 10797114. DOI: 10.1103/PhysRevLett.82.414.

[138] Pamela T. Korda, Michael B. Taylor, and David G. Grier. "Kinetically Locked-In Colloidal Transport in an Array of Optical Tweezers". In: *Physical Review Letters* 89.12 (2002), p. 128301. ISSN: 10797114. DOI: 10.1103/PHYSREVLETT.89.128301/FIGURES/5/MEDIUM.

[139] Thomas Bohlein and Clemens Bechinger. "Experimental observation of directional locking and dynamical ordering of colloidal monolayers driven across quasiperiodic substrates". In: *Physical Review Letters* 109.5 (2012), p. 058301. ISSN: 00319007. DOI: 10.1103/PHYSREVLETT.109.058301/FIGURES/5/MEDIUM.

[140] C. Reichhardt and C. J.Olson Reichhardt. "Random organization and plastic depinning". In: *Physical Review Letters* 103.16 (2009), p. 168301. ISSN: 00319007. DOI: 10.1103/PHYSREVLETT.103.168301/FIGURES/4/MEDIUM. arXiv: 0812.3425. URL: https://journals.aps.org/prl/abstract/10.1103/PhysRevLett.103.168301.

[141] Pietro Tierno. "Depinning and collective dynamics of magnetically driven colloidal monolayers". In: *Physical Review Letters* 109.19 (2012), p. 198304. ISSN: 00319007. DOI: 10.1103/PHYSREVLETT.109.198304/FIGURES/4/MEDIUM.

[142] Thomas Bohlein, Jules Mikhael, and Clemens Bechinger. "Observation of kinks and antikinks in colloidal monolayers driven across ordered surfaces". In: *Nature Materials* 11.2 (2011), pp. 126–130. ISSN: 1476-4660. DOI: 10.1038/nmat3204.

[143] Ralf Eichhorn, Peter Reimann, and Peter Hänggi. "Brownian Motion Exhibiting Absolute Negative Mobility". In: *Physical Review Letters* 88.19 (2002), p. 190601. ISSN: 10797114. DOI: 10.1103/PhysRevLett.88.190601. arXiv: 0204367 [cond-mat].

[144] Sven Matthias and Frank Müller. "Asymmetric pores in a silicon membrane acting as massively parallel brownian ratchets". In: *Nature* 424.6944 (2003), pp. 53–57. ISSN: 1476-4687. DOI: 10.1038/nature01736.

[145] Alexandra Ros et al. "Absolute negative particle mobility". In: *Nature* 436.7053 (2005), pp. 928–928. ISSN: 1476-4687. DOI: 10.1038/436928a.

[146] Danielle McDermott, Cynthia J. Olson Reichhardt, and Charles Reichhardt. "Collective ratchet effects and reversals for active matter particles on quasi-one-dimensional asymmetric substrates". In: *Soft Matter* 12.41 (2016), pp. 8606–8615. ISSN: 1744-6848. DOI: 10.1039/C6SM01394E.

[147] Sang Hyuk Lee et al. "Observation of flux reversal in a symmetric optical thermal ratchet". In: *Physical Review Letters* 94.11 (2005), p. 110601. ISSN: 00319007. DOI: 10.1103/PHYSREVLETT.94.110601/FIGURES/2/MEDIUM.

[148] Christian Schwemmer et al. "Experimental Observation of Current Reversal in a Rocking Brownian Motor". In: *Physical Review Letters* 121.10 (2018), p. 104102. ISSN: 10797114. DOI: 10.1103/PHYSREVLETT.121.104102/FIGURES/4/MEDIUM. arXiv: 1805.03993.

[149] P. G. Drazin and R. S. Johnson. *Solitons: An Introduction*. Cambridge University Press, 1989. ISBN: 9780521336550. DOI: 10.1017/CBO9781139172059.

[150] Tarik Yefsah et al. "Heavy solitons in a fermionic superfluid". In: *Nature* 499.7459 (2013), pp. 426–430. ISSN: 1476-4687. DOI: 10.1038/nature12338. arXiv: 1302.4736.

[151] Kevin E. Strecker et al. "Formation and propagation of matter-wave soliton trains". In: *Nature* 417.6885 (2002), pp. 150–153. ISSN: 1476-4687. DOI: 10.1038/nature747.

[152] Jason H.V. Nguyen, De Luo, and Randall G. Hulet. "Formation of matter-wave soliton trains by modulational instability". In: *Science* 356.6336 (2017), pp. 422–426. ISSN: 10959203. DOI: 10.1126/SCIENCE.AAL3220/SUPPL_FILE/AAL3220_NGUYEN_SM.PDF. arXiv: 1703.04662.

[153] E. Sharon, G. Cohen, and J. Fineberg. "Propagating solitary waves along a rapidly moving crack front". In: *Nature* 410.6824 (2001), pp. 68–71. ISSN: 1476-4687. DOI: 10.1038/35065051.

[154] Andrea Costa et al. "Soliton turbulence in shallow water ocean surface waves". In: *Physical Review Letters* 113.10 (2014), p. 108501. ISSN: 10797114. DOI: 10.1103/PHYSREVLETT.113.108501/FIGURES/7/MEDIUM. arXiv: 1407.1021.

[155] Michael P.N. Juniper et al. "Microscopic dynamics of synchronization in driven colloids". In: *Nature Communications* 6.1 (2015), pp. 1–7. ISSN: 2041-1723. DOI: 10.1038/ncomms8187.

[156] Pietro Tierno and Thomas M. Fischer. "Excluded volume causes integer and fractional plateaus in colloidal ratchet currents". In: *Physical Review Letters* 112.4 (2014), p. 048302. ISSN: 00319007. DOI: 10.1103/PHYSREVLETT.112.048302/FIGURES/4/MEDIUM.

[157] G. Gerber et al. "Particle-Size-Exclusion Clogging Regimes in Porous Media". In: *Physical Review Letters* 120.14 (2018), p. 148001. ISSN: 10797114. DOI: 10.1103/PHYSREVLETT.120.148001/FIGURES/4/MEDIUM.

[158] G. Gerber et al. "Self-Limited Accumulation of Colloids in Porous Media". In: *Physical Review Letters* 123.15 (2019), p. 158005. ISSN: 10797114. DOI: 10.1103/PHYSREVLETT.123.158005/FIGURES/3/MEDIUM.

[159] Navid Bizmark et al. "Multiscale dynamics of colloidal deposition and erosion in porous media". In: *Science Advances* 6.46 (2020), pp. 2530–2543. ISSN: 23752548. DOI: 10.1126/SCIADV.ABC2530/SUPPL_FILE/ABC2530_SM.PDF.

[160] T. Matsuda et al. "Oscillating Rows of Vortices in Superconductors". In: *Science* 294.5549 (2001), pp. 2136–2138. ISSN: 00368075. DOI: 10.1126/SCIENCE.1065968.

[161] Heng Wu et al. "The field-free Josephson diode in a van der Waals heterostructure". In: *Nature* 604.7907 (2022), pp. 653–656. ISSN: 1476-4687. DOI: 10.1038/s41586-022-04504-8.

[162] Tapomoy Bhattacharjee and Sujit S. Datta. "Bacterial hopping and trapping in porous media". In: *Nature Communications* 10.1 (2019), pp. 1–9. ISSN: 2041-1723. DOI: 10.1038/s41467-019-10115-1.

[163] O. J. Meacock et al. "Bacteria solve the problem of crowding by moving slowly". In: *Nature Physics* 17.2 (2021), pp. 205–210. ISSN: 1745-2481. DOI: 10.1038/s41567-020-01070-6. arXiv: 2008.07915.

[164] Amin Dehkharghani, Nicolas Waisbord, and Jeffrey S. Guasto. "Self-transport of swimming bacteria is impaired by porous microstructure". In: *Communications Physics 2023 6:1* 6.1 (2023), pp. 1–9. ISSN: 2399-3650. DOI: 10.1038/s42005-023-01136-w. arXiv: 2201.03059.

[165] Markus Kollmann. "Single-file Diffusion of Atomic and Colloidal Systems: Asymptotic Laws". In: *Physical Review Letters* 90.18 (2003), p. 180602. ISSN: 10797114. DOI: 10.1103/PhysRevLett.90.180602. arXiv: 0211562 [cond-mat].

[166] Alessandro Taloni and Fabio Marchesoni. "Single-file diffusion on a periodic substrate". In: *Physical Review Letters* 96.2 (2006), p. 020601. ISSN: 10797114. DOI: 10.1103/PHYSREVLETT.96.020601/FIGURES/3/MEDIUM.

[167] Fabio Marchesoni and Alessandro Taloni. "Subdiffusion and long-time anticorrelations in a stochastic single file". In: *Physical Review Letters* 97.10 (2006), p. 106101. ISSN: 00319007. DOI: 10.1103/PHYSREVLETT.97.106101/FIGURES/4/MEDIUM.

[168] L. Lizana and T. Ambjörnsson. "Single-file diffusion in a box". In: *Physical Review Letters* 100.20 (2008), p. 200601. ISSN: 00319007. DOI: 10.1103/PHYSREVLETT.100.200601/FIGURES/4/MEDIUM. arXiv: 0801.0563.

[169] Alexis Poncet et al. "Generalized Correlation Profiles in Single-File Systems". In: *Physical Review Letters* 127.22 (2021), p. 220601. ISSN: 10797114. DOI: 10.1103/PHYSREVLETT.127.220601/FIGURES/3/MEDIUM.

[170] Alejandro Villada-Balbuena et al. "Single-file dynamics of colloids in circular channels: Time scales, scaling laws and their universality". In: *Physical Review Research* 3.3 (2021), p. 033246. ISSN: 26431564. DOI: 10.1103/PHYSREVRESEARCH.3.033246/FIGURES/7/MEDIUM.

Index